remote sensing

MDPI

Article

Integrating Surface Deformation and Ecological Indicators for Mining Environment Assessment: A Novel MDECI Approach

Lei Zhang [1,2,3], Qiaomei Su [1], Bin Zhang [1,2,3,*], Hongwen Xue [4], Zhengkang Zuo [1], Yanpeng Li [2,5] and He Zheng [2,5]

1 College of Geological and Surveying Engineering, Taiyuan University of Technology, Taiyuan 030024, China
2 Key Laboratory of Ionic Rare Earth Resources and Environment, Ministry of Natural Resources of the People's Republic of China, Ganzhou 341000, China
3 Engineering Technology Innovation Center for Ecological Protection and Restoration in the Middle Yellow River, Ministry of Natural Resources, Taiyuan 030024, China
4 The Third Geological Exploration Institute of China Metallurgical Geology Bureau, Taiyuan 030032, China
5 School of Geomatics and Geoinformation, Jiangxi College of Applied Technology, Ganzhou 341000, China
* Correspondence: binzhang@tyut.edu.cn

Highlights

What are the main findings?

- A Mining Deformation–Ecology Coupling Index (MDECI) was developed by integrating InSAR-derived surface stability with multi-spectral indicators.
- A non-linear "unimodal" response mechanism was identified in the Datong Coalfield, revealing an Ecological Turning Point (ETP) at −100 mm where mining ecosystems transition to structural degradation.

What are the implications of the main findings?

- MDECI significantly outperforms traditional models by maintaining a stable Average Correlation Coefficient (ACC) of 0.63–0.75, achieving a 30.3% performance lead (0.628 vs. 0.482) during environmental interference while remaining highly consistent with existing benchmarks (correlation > 0.9).
- The −100 mm threshold establishes a quantitative boundary for mining intensity control, providing an early-warning basis to prevent ecosystems from crossing the degradation turning point.

Abstract

Surface subsidence induced by underground coal mining is a primary driver of ecological degradation. The traditional Remote Sensing Ecological Index (RSEI), however, struggles to capture surface deformation constraints and vegetation response lags. To address this, we developed a Mining Deformation–Ecology Coupling Index (MDECI). This index integrates Interferometric Synthetic Aperture Radar (InSAR)-monitored surface stability with multi-spectral indicators via Principal Component Analysis (PCA). We applied this method to the Datong Coalfield, China, using 231 Sentinel-1A SAR scenes and 8 Landsat images (2017–2024) to validate the effectiveness of the index. Meanwhile, we systematically analyzed non-linear response mechanisms, the Ecological Turning Point (ETP), and spatial clustering characteristics. The results demonstrate the following: (1) InSAR and MDECI effectively identified patterns of surface subsidence and ecological decline. Subsidence centers expanded to a maximum of −2085 mm, causing the mean MDECI in these areas to drop to 0.185 (<−1800 mm). This represents a 57.4% decrease relative to the regional average (0.434). (2) MDECI outperformed traditional models with a stable Average Correlation Coefficient (ACC) (0.63–0.75) and high cross-correlation

Check for updates

Academic Editor: Antonio Miguel Ruiz Armenteros

Received: 9 March 2026
Revised: 12 April 2026
Accepted: 20 April 2026
Published: 22 April 2026

Copyright: © 2026 by the authors. Licensee MDPI, Basel, Switzerland. This article is an open access article distributed under the terms and conditions of the Creative Commons Attribution (CC BY) license.

coefficients with RSEI (0.906) and the Mine-specific Eco-environment Index (MSEEI) (0.931). During the 2018 drought, MDECI maintained a robust ACC of 0.628 while RSEI dropped to 0.482. (3) Multi-scale analysis revealed a unimodal MDECI response with an ETP at −100 mm. Initial 'micro-disturbance gain' (0.371 to 0.471) is followed by a progressive decline to a minimum of 0.185 under severe deformation. (4) Local Indicators of Spatial Association (LISA) spatial clustering characterized the distribution patterns of ecological damage and localised high-maintenance areas. High–Low damaged areas accounted for 5.09%, while High–High high-maintenance areas reached 9.00%. The scale of High–High areas was approximately 1.77 times that of the damaged areas. The MDECI addresses the deficiencies of traditional indices in high-disturbance areas and isolates the impact of mining on the ecology, providing a quantitative basis for risk identification and differentiated restoration.

Keywords: InSAR; coal mining subsidence; subsidence-driven ecological degradation; Mining Deformation–Ecology Coupling Index

1. Introduction

Coal mining is widely recognised as a major driver of surface deformation and ecological degradation. These environmental impacts are particularly significant in regions with scarce water resources and fragile ecosystems. Surface subsidence induced by underground mining directly damages soil structure and weakens water retention. It also alters the spatial redistribution of nutrients, thereby accelerating soil degradation and inhibiting vegetation growth [1,2]. In the Loess Plateau and other mining areas, limited precipitation and slow natural recovery amplify these mining-induced deformation disturbances. Consequently, regional ecosystems exhibit heightened sensitivity to long-term underground mining activities [3]. Existing studies show that subsidence reshapes landforms and significantly affects vegetation distribution and ecosystem stability [4,5]. This highlights the fundamental role of surface deformation as a deformation constraint in ecological evolution. Therefore, understanding how mining-induced deformation affects ecosystems is crucial for accurate impact assessment and sustainable management.

Although remote sensing is widely used for monitoring mining environments, most studies focus on multi-spectral imagery to construct vegetation or ecological indices. The Remote Sensing Ecological Index (RSEI) is considered effective for reflecting multi-dimensional information, including vegetation, moisture, heat, and bare soil [6]. A researcher has modified RSEI for mining environments and integrated driver analysis to reveal influence mechanisms [7]. Recently, RSEI and its variants have been applied to specific mining cases to reveal spatial heterogeneity and evolution [8,9]. These studies confirm the significant disturbance effects of mining at a macro level. However, relying solely on optical indices in high-intensity underground mining areas has limitations. Vegetation spectral responses often lag behind rapid surface structural alterations. This makes it difficult to reflect crack development and surface structural damage in a timely manner. Furthermore, ecosystem responses often exhibit non-linear characteristics under different disturbance intensities. Traditional indices may overestimate or underestimate ecological status in strong subsidence areas [10]. To address this, current research suggests moving beyond single optical datasets by introducing deformation constraint information that directly characterises disturbance intensity and structural status [11].

Interferometric Synthetic Aperture Radar (InSAR) offers distinct advantages for monitoring surface subsidence and structural damage. It provides high-precision deformation data regardless of light or weather conditions [12]. Studies demonstrate that InSAR effectively characterises subsidence range, deformation rates, and spatio-temporal evolution [13]. It serves as a reliable means for identifying high-disturbance areas and assessing surface stability. With the advancement of time-series InSAR, the consistency of long-term monitoring has improved [14–16]. This allows for a clearer characterisation of the cumulative impacts of underground mining. Research increasingly recognises that surface deformation is a direct response to mining. It often correlates strongly with ecological changes such as vegetation degradation and habitat fragmentation [17,18]. This provides a new perspective for supplementing ecological evaluation with deformation process data.

In summary, traditional optical indices have limitations in underground mining environments. They struggle to fully reflect the direct constraints of disturbances like subsidence and cracks. Therefore, this paper proposes a Mining Deformation–Ecology Coupling Index (MDECI). We introduce InSAR-monitored surface deformation as a deformation constraint into the ecological evaluation framework. This allows the index to reflect both multispectral ecological responses and surface structural variations caused by deformation. Based on MDECI and Small Baseline Subset Interferometric Synthetic Aperture Radar (SBAS-InSAR) data, we conducted gradient zoning and Bivariate Local Indicators of Spatial Association (LISA) spatial clustering analysis. This quantified ecological evolution across different deformation intensities and revealed spatial patterns. In Datong Coalfield, this research aims to provide a reliable quantitative method for ecological monitoring in high-disturbance areas. It also offers a scientific basis for ecological restoration and risk management in mining regions.

2. Study Area and Data

2.1. Study Area

The study area (Figure 1) is situated in the Datong Coalfield, northern Shanxi Province, China (112.56°E–113.42°E, 39.73°N–40.22°N). It lies on the north-eastern edge of the Loess Plateau, where the topography transitions from loess hills and gullies in the north-west to alluvial plains in the south-east. The region has an average elevation of approximately 1279 m and a typical semi-arid continental monsoon climate. Meteorological statistics from 2017 to 2024 indicate a mean annual temperature of 7.2 °C and mean annual precipitation of 559.7 mm. Rainfall is primarily concentrated from June to September. However, the annual potential evaporation reaches 1901.7 mm, resulting in a significant water deficit [19]. Under these climatic and topographical conditions, vegetation growth is highly dependent on soil moisture. Consequently, the regional ecosystem is sensitive to both drought and surface deformation disturbances. The vegetation mainly consists of artificial forests and natural shrubs or grasses [20]. The Datong Coalfield is a Jurassic-Carboniferous-Permian composite coalfield. It hosts several ultra-large mines, such as Tashan and Tongxin, with annual capacities exceeding ten million tonnes. Long-term, high-intensity underground mining has induced widespread surface subsidence and crack development [19]. Surface deformation in this area is primarily driven by goaf collapse. This process directly damages soil structure and alters the structural conditions of the growing environment for vegetation [21,22].

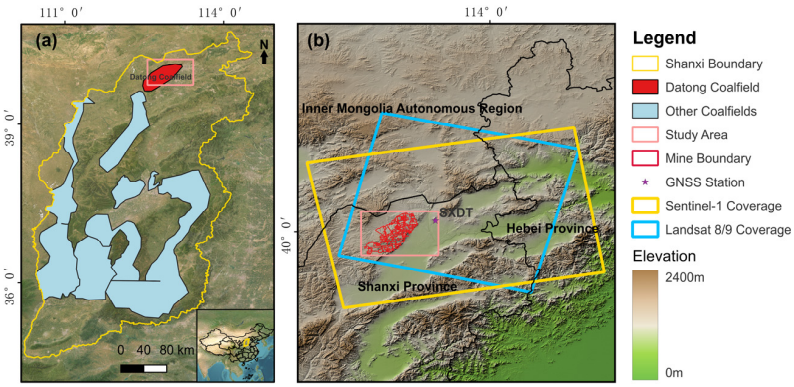

Figure 1. Overview of the study area: (**a**) Geographical location of the Datong Coalfield in Shanxi Province, China; (**b**) Topographic map of the study area, showing the boundaries of the mining area, the location of the SXDT GNSS station, and the spatial coverage of Sentinel-1 (yellow rectangle) and Landsat 8/9 (blue rectangle) data.

2.2. Data

2.2.1. SAR Data

This study utilised Sentinel-1A (S-1A) Synthetic Aperture Radar (SAR) Single Look Complex (SLC) data for surface deformation monitoring. A total of 231 scenes were collected for the Datong Coalfield, spanning the period from March 2017 to December 2024. The parameter information for the S-1A data is presented in Table 1. Corresponding Precise Orbit Ephemerides (POE) were utilised to refine the orbital parameters [23,24].

Table 1. Parameter specifications of the SAR data utilized in this study.

Orbit Type	Path	Polarization	Data Mode	Azimuth Angle	Incidence Angle
Ascending	40	VV	IW	346.5°	35.5°

2.2.2. Optical Data

This study acquired Landsat 8 Operational Land Imager/Thermal Infrared Sensor (OLI/TIRS) and Landsat 9 OLI-2/TIRS-2 Level-2 Surface Reflectance products spanning 2017 to 2024 [25]. To mitigate the impact of seasonal phenological variations on ecological evaluation, only imagery from the annual vegetation growing season (June–September) was selected to characterize ecological quality. Through cloud removal and the application of a median composition algorithm, a total of eight cloud-free composite images-one for each year from 2017 to 2024-were generated [26].

2.2.3. Auxiliary Data

To ensure the precision of InSAR data processing and to facilitate reliability validation and causal analysis, the following four categories of auxiliary data were integrated into this study:

(1) Atmospheric Correction Data: To address the unavoidable tropospheric delay errors in interferometry, this study introduced high-resolution global Zenith Total Delay (ZTD) data provided by the Generic Atmospheric Correction Online Service (GACOS) [27,28]. These data, generated based on European Centre for Medium-Range Weather Forecasts (ECMWF) numerical weather models, served as an external correction source within the SBAS-InSAR workflow to overwhelm atmospheric phase errors.

(2) SRTM Data: The Shuttle Radar Topography Mission (SRTM) Digital Elevation Model (DEM) provided by National Aeronautics and Space Administration (NASA) was utilized [29]. The SRTM data was utilised for topographic phase removal during SBAS-

InSAR processing and for the final geocoding of the deformation results. Its spatial resolution is 30 m.

(3) In-Situ Validation Data: To evaluate the accuracy of the InSAR monitoring results, daily Global Navigation Satellite System (GNSS) observation data (2017–2023) from the Continuously Operating Reference Station SXDT located within the study area were collected [30]. By projecting the three-dimensional deformation components obtained via GNSS onto the radar Line of Sight (LOS), point-to-point accuracy validation was performed between the remote sensing inversion results and ground-truth values.

(4) GIS Vector Data: Vector data representing the mining boundaries of major mines in the Datong Coalfield were gathered. These data were spatially overlaid with the InSAR deformation fields and the MDECI to analyze the spatial relationships between surface deformation and ecological quality across the study region.

3. Methods

The technical framework developed in this study is illustrated in Figure 2. First, within the Sentinel-1A data processing module, high-precision absolute cumulative deformation time series were inverted using the SBAS-InSAR technique, integrated with GACOS atmospheric correction and Ground Control Points (GCPs)-based orbital refinement (see Section 3.1). Simultaneously, rigorous pre-processing was performed on Landsat 8/9 imagery within the MDECI model construction module. Subsequently, during the evaluation indicator system construction phase, four ecological indicators—Greenness (Modified Soil Adjusted Vegetation Index, MSAVI), Wetness (Normalized Difference Moisture Index, NDMI), Dryness (Normalized Difference Built-up and Soil Index, NDBSI), and Heat (Land Surface Temperature, LST)—were calculated. The InSAR deformation results were then transformed into an Instability indicator to represent the surface structural status. These five indicators were integrated using Principal Component Analysis (PCA) to construct the MDECI (see Section 3.2). Following this, analytical methods, including gradient-based subzoning statistics and LISA, were applied. These were utilised to comprehensively reveal the spatio-temporal evolution and coupled response patterns of the ecological environment within the mining area (see Section 3.3). Finally, accuracy validation of the SBAS-InSAR results and performance evaluation of the MDECI model were conducted (see Section 3.4).

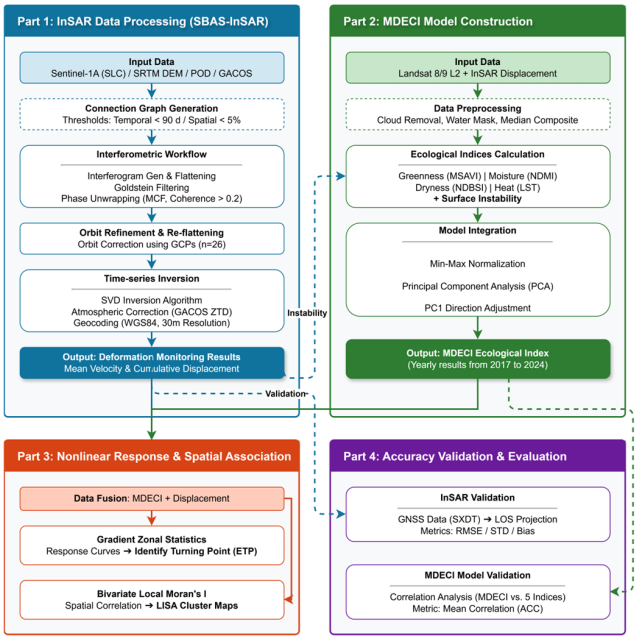

Figure 2. Technical flowchart of the research.

3.1. InSAR Data Processing

This study adopted the Small Baseline Subset (SBAS-InSAR) technique to acquire long-term surface deformation information for the study area. The core of this technique involves establishing spatiotemporal baseline thresholds to construct an interferometric topological network with high redundancy, thereby effectively overcoming spatiotemporal decorrelation effects [12]. Assuming that $N+1$ SAR images were acquired for the same monitoring area at times $t_0, \ldots, t_N$, the number of generated differential interferograms M must satisfy the following constraint:

$$\frac{N+1}{2} \leq M \leq \frac{N(N+1)}{2} \tag{1}$$

For the j-th ($j = 1, \ldots, M$) interferometric pair, the physical observation model of the interferometric phase $\delta\phi_j$ can be expressed as a linear superposition of the LOS deformation phase and various error phase components [12]:

$$\delta\phi_j(x,r) \approx \frac{4\pi}{\lambda}[d(t_B,x,r) - d(t_A,x,r)] + \Delta\phi_{topo,j} + \Delta\phi_{atm,j} + \Delta n_j \tag{2}$$

where (x,r) represents the pixel coordinates, λ is the radar wavelength, $d(t_B)$ and $d(t_A)$ separately denote the cumulative LOS deformation at times t_B and t_A, respectively, and $\Delta\phi_{topo,j}$, $\Delta\phi_{atm,j}$, and Δn_j represent the residual topographic phase, atmospheric delay phase, and noise phase components, respectively.

In the specific data processing workflow, an external digital elevation model (SRTM DEM) was utilized to remove the reference topographic phase. Furthermore, ZTD data provided by GACOS were introduced to correct the tropospheric delay for each scene $\Delta\phi_{atm,j}$ [30]. Subsequently, adaptive filtering was applied to suppress noise interference, and the Minimum Cost Flow algorithm was employed for phase unwrapping [31]. Orbital refinement and re-flattening were then performed using high-coherence GCPs to eliminate residual phase trends caused by orbital residuals or topographic errors.

To further derive a continuous deformation evolution rate, the entire sequence of observations was integrated into a linear matrix equation based on the average deformation rate v for each time interval:

$$Bv = \delta\phi \tag{3}$$

where B is an $M \times N$ coefficient matrix, M denotes the number of generated and quality-qualified interferograms, and N refers to the number of adjacent time intervals divided by the $N+1$ images. The Singular Value Decomposition algorithm [12] was employed to solve the generalized inverse of the equation system. This allowed for the joint processing of different small baseline subsets to obtain the optimal estimate of the surface deformation rate under the minimum norm criterion. Finally, the full-sequence cumulative deformation was obtained through temporal accumulation and geocoded into a unified geographic coordinate system to achieve a spatial quantitative representation of the deformation monitoring results.

3.2. Mining Deformation–Ecology Coupling Index (MDECI)

To address the limitations of the traditional RSEI [32], which primarily focuses on natural surface cover while neglecting geological deformation stresses specific to mining areas, this study—grounded in the "Pressure-State-Response" framework—integrates the Instability indicator representing surface structural status with the four dimensions of greenness, wetness, dryness, and heat. Consequently, we innovatively proposed the MDECI. Specifically, greenness, wetness, dryness, and heat were derived from optical imagery, while the surface instability indicator was obtained from SAR time-series analysis.

Prior to calculating the optical indicators, a rigorous pre-processing workflow was implemented on Landsat 8/9 Level-2 Surface Reflectance products. Pixel-level quality control was performed using the Quality Assessment (QA) band to mask clouds, cloud shadows, and radiometric saturation pixels. Subsequently, a median composition algorithm was applied to reconstruct growing-season imagery, eliminating residual atmospheric noise and filling data gaps. Finally, the Modified Normalized Difference Water Index (MNDWI) was utilized to mask water bodies, ensuring the accuracy of terrestrial ecological evaluation.

The MDECI model couples surface deformation with ecological indicators, including Greenness (MSAVI), Wetness (NDMI), Dryness (NDBSI), and Heat (LST). To ensure a focused presentation of the methodological innovations and enhance readability, the specific mathematical formulations for these four established indicators are provided in Appendix A (Table A1). Finally, PCA was introduced to determine the weights of each component, integrating these factors to generate the final MDECI, which more objectively reflects the spatiotemporal evolution of ecological quality in the study area.

3.2.1. Instability Indicator

Utilizing the surface deformation values derived in Section 3.1, this study develops the Instability indicator to precisely quantify the net annual surface structural disturbance of the land surface. An annual increment method is employed, which calculates the absolute difference between the cumulative deformation at the end and the beginning of each year. This approach isolates the magnitude of surface activity for the current year by stripping away historical cumulative effects. The calculation formula is as follows:

$$Instability = \left| D_{end,i} - D_{start,i} \right| \tag{4}$$

where $D_{end,i}$ and $D_{start,i}$ represent the LOS cumulative deformation values at the end and the beginning of year i, respectively. The choice of absolute deformation increments is grounded in regional geology and modeling requirements. Specifically, subsidence dominates the Datong Coalfield with negligible uplift, making absolute values a consistent proxy for deformation disturbance intensity. Furthermore, this approach ensures a unidirectional scale where zero represents absolute stability and higher values consistently indicate increased structural disturbance, establishing the monotonicity that is a mathematical prerequisite for the robust performance of the subsequent Principal Component Analysis (PCA). By ensuring this unidirectional relationship, the model can assign consistent and interpretable loading weights to the Instability indicator, thereby guaranteeing that higher indicator values reliably represent poorer ecological status across the study area.

3.2.2. Principal Component Analysis and MDECI Synthesis

Due to the inconsistent units and scales of the five indicators—Greenness (MSAVI), Wetness (NDMI), Dryness (NDBSI), Heat (LST), and surface Instability—this study employs PCA [33] for integration. To eliminate dimensional differences and mitigate the interference of extreme pixels on the model, a standardization process is first applied to each indicator. Following a statistical distribution criterion, the effective values of each indicator are clipped within the range of the mean plus or minus three standard deviations ($\mu \pm 3\sigma$), and subsequently mapped linearly to the interval $[0, 1]$. An orthogonal transformation is then performed on the multidimensional space using the covariance matrix, automatically allocating loading weights based on the contribution of each indicator to the dataset's variance. This process avoids the subjective bias of manual weighting and effectively eliminates information redundancy between indicators [32].

The first principal component (PC1) typically aggregates the majority of the characteristic information from the variables and serves as a comprehensive representative of the regional ecological environment. Among the indicators, MSAVI and NDMI exert a positive promotional effect on ecological quality, while NDBSI, LST, and Instability exert a negative inhibitory effect. If the calculated PC1 loadings are opposite to the aforementioned ecological significance (i.e., high values representing poor ecology), a directional correction is executed [32] to construct the initial ecological index ($MDECI_0$) (Equation (5)):

$$MDECI_0 = 1 - PC1[f(MSAVI, NDMI, NDBSI, LST, Instability)] \quad (5)$$

Finally, to ensure the comparability of monitoring results across different years (2017–2024), a linear normalisation is applied to the results. This yields $MDECI$ with a value range of [0,1] (Equation (6)):

$$MDECI = (MDECI_0 - MDECI_{min})/(MDECI_{max} - MDECI_{min}) \quad (6)$$

where $MDECI_{min}$ and $MDECI_{max}$ are the minimum and maximum values of the index, respectively. A $MDECI$ value closer to 1 indicates better ecological environmental quality, whereas a value closer to 0 indicates poorer quality.

3.3. Non-Linear Response and Spatial Association Analysis Between Surface Deformation and Ecological Quality

The other aim of this study is quantify the spatial interaction between surface deformation and ecological quality. To comprehensively evaluate the cumulative ecological effects of long-term mining activities in the study area, we selected the cumulative subsidence and MDECI for 2024 (the end of the monitoring period) as the primary objects of analysis. The rationale for this selection is based on the following: (1) Surface subsidence is a continuous and cumulative process. Only the cumulative data at the end of the period can fully represent the ultimate degree of surface damage. (2) Ecosystems exhibit a "time-lag effect" in response to environmental changes. The ecological state in 2024 is a synthesized result of continuous damage over the preceding years, rather than a transient manifestation of a single year. (3) By 2024, the previously scattered subsidence points in the study area had merged into large-scale subsidence areas, forming a complete subsidence gradient from the center to the periphery. This provides the most robust sample size for identifying spatial regularities. Based on this data foundation, this study employs gradient-based zonal statistics and LISA to conduct the specific analyses.

3.3.1. Ecological Damage Response Mechanism and Turning Point Identification

This study integrates ecological gradient analysis theory [34] with GIS-based zonal statistics [35] to characterize the staged ecological response to surface deformation. Using the 2017–2024 cumulative subsidence as the spatial constraint baseline, the study area was discretized into multi-scale objective gradients to balance spatial sensitivity and statistical robustness. A 100 mm interval was applied to the sensitive zones (0 to −1000 mm) to precisely identify the Ecological Turning Point (ETP) [36]—the critical peak where the ecosystem transitions from 'micro-disturbance gain' to 'progressive degradation'. For the severe subsidence zones (<−1000 mm), the intervals were adaptively expanded (up to 400 mm) to suppress statistical noise arising from the sparse pixel samples in extreme deformation areas. Mean values of MDECI were extracted for each gradient to construct a continuous "subsidence-ecology" response curve.

3.3.2. Detection of Deformation-Ecological Spatial Association Patterns

To investigate the spatial interaction between the surface damage intensity at the end of the mining period and the state of the ecological system from a spatial perspective, this study introduced the bivariate Local Moran's I [37]. By detecting the spatial correlation between the absolute cumulative subsidence and the MDECI as of 2024, a LISA cluster map was generated. This method effectively identifies the synergistic effects and abnormal aggregation characteristics of long-term surface deformation and ecological response in space, thereby revealing the spatial driving mechanism of the final state of surface damage on regional ecological quality. The calculation formula is as follows (Equation (7)):

$$I_i^{kl} = z_i^k \sum_{j=1, j \neq i}^{n} w_{ij} z_j^l \tag{7}$$

where I_i^{kl} is the bivariate local Moran's I at pixel i, w_{ij} denotes the row-standardised spatial weight matrix constructed based on the Queen's contiguity criterion, which represents the spatial connection strength between pixels, i and j denote the spatial indices of the central pixel and its neighbours, respectively, k and l represent two distinct variable components, namely the cumulative subsidence and the PCRSEI, z_i^k is the standardised value (Z-score) of variable k at position i, and z_j^l is the standardised value of variable l at the neighbouring position j.

Based on the calculation results, the study area is categorized into five spatial association modes with distinct significance. The Not Significant (0) regions represent areas where no statistically significant association between surface deformation and ecological quality is observed. The other four significant cluster modes are defined as follows:

(1) High-Low (HL) Cluster: High cumulative subsidence corresponds to low ecological quality. This mode identifies ecologically damaged areas severely affected by mining-induced disturbances.

(2) High-High (HH) Cluster: High cumulative subsidence corresponds to high ecological quality. This represents high-ecology maintenance areas despite a background of intense subsidence.

(3) Low-Low (LL) Cluster: Low subsidence corresponds to low ecological quality. This represents the baseline ecological environment that is not significantly disturbed by subsidence but is limited by natural geomorphological conditions.

(4) Low-High (LH) Cluster: Low subsidence corresponds to high ecological quality. This represents the baseline ecological environment with good vegetation cover that remains unaffected by subsidence.

To quantitatively characterize the scale and structure of ecological damage and restoration compensation in the mining area, this study extracts the pixel frequency of each mode from the LISA cluster maps and calculates their percentage relative to the total area of the study region. This reveals the spatial coverage level and ecological response degree of mining disturbances at the regional scale.

3.4. Accuracy Validation and Model Effectiveness Evaluation

To ensure the reliability of the research findings, this study separately validated and evaluated the accuracy of the InSAR monitoring results and the performance of the MDECI model.

3.4.1. InSAR Accuracy Validation

To verify the precision of the derived deformation results, continuous GNSS observation data from the SXDT station within the study area were utilized. Its location is

indicated in Figure 1b. Following the projection method proposed by Hanssen (2001) [38], the three-dimensional GNSS deformation components were converted into the radar LOS direction using Equation (8):

$$d_{LOS} = d_u cos\theta - d_e sin\theta cos\alpha_h + d_n sin\theta sin\alpha_h \quad (8)$$

where d_{LOS} is the LOS deformation, d_u, d_n, and d_e represent the vertical, north–south, and east–west displacement components of the GNSS, respectively, θ is the radar incidence angle, and α_h is the satellite flight heading angle (measured clockwise from the North).

The projected GNSS LOS deformation time series were compared with the InSAR deformation results from the pixel nearest to the GNSS station. Quantitative assessment of the InSAR deformation accuracy was conducted by calculating statistical metrics, including the Standard Deviation (STD) and Root Mean Square Error (RMSE).

3.4.2. Performance Validation of MDECI

Since regional ecological quality is difficult to obtain through direct in situ ground measurements for validation, this study utilizes the average correlation degree to evaluate the performance of the MDECI index [39]. According to evaluation theory, a robust composite index should maintain high correlation with each of its component indicators, demonstrating that it effectively summarizes multi-dimensional ecological information [32].

In this study, the Pearson Correlation Coefficient was utilized to calculate the correlation between MDECI and its five component indicators (MSAVI, NDMI, NDBSI, LST, and Instability) from 2017 to 2024, and the Average Correlation Coefficient (ACC) was constructed. The calculation formula is as follows:

$$R_i = \frac{\sum_{k=1}^{n}(x_k - \overline{x})(y_k - \overline{y})}{\sqrt{\sum_{k=1}^{n}(x_k - \overline{x})^2}\sqrt{\sum_{k=1}^{n}(y_k - \overline{y})^2}} \quad (9)$$

$$\overline{R} = \frac{1}{m}\sum_{i=1}^{m}|R_i| \quad (10)$$

where R_i is the correlation coefficient between MDECI and the i-th component indicator, $\overline{R}$ is ACC, and m is the total number of indicators ($m = 5$ in this study). If the $\overline{R}$ value of MDECI is higher than that of the traditional RSEI or other comparative models, it proves that after introducing the surface instability indicator, the improved model does not lose its explanatory power for natural ecological information. Instead, it becomes more suitable for mining environments due to the inclusion of deformation constraints.

4. Results

4.1. Spatiotemporal Evolution Characteristics of Surface Deformation

Following the SBAS-InSAR processing workflow described in Section 3.1, this study selected and processed 231 Sentinel-1A ascending orbit scenes. As shown in the temporal baseline plot (Figure 3), a total of 345 interferometric pairs were generated to ensure high coherence. The blue pentagram in Figure 3 identifies the super-master image acquired on 5 March 2021, which serves as the reference for both temporal and perpendicular baselines. To provide a reliable deformation datum, a spatial reference point (red triangle) was established in a stable area in the northeastern part of the study area (as indicated in Figure 4).

The monitoring results (Figure 4) indicate that the annual average deformation rate of the Datong Coalfield for the 2017–2024 period exhibits significant spatial heterogeneity. Subsidence centers are highly concentrated above the underground fully mechanized

longwall mining faces of mines such as Yanzishan, Tongxin, and Tashan, forming a typical "multi-center funnel" pattern. This spatial distribution objectively reflects the violent surface disturbances caused by the collapse of overlying strata due to high-intensity mining activities. Statistical analysis reveals that the maximum annual average subsidence rate in the region reached −256.57 mm/year. This extreme center is located at the characteristic point P1 within the subsidence funnel, where the cumulative subsidence during the monitoring period has exceeded −2000 mm.

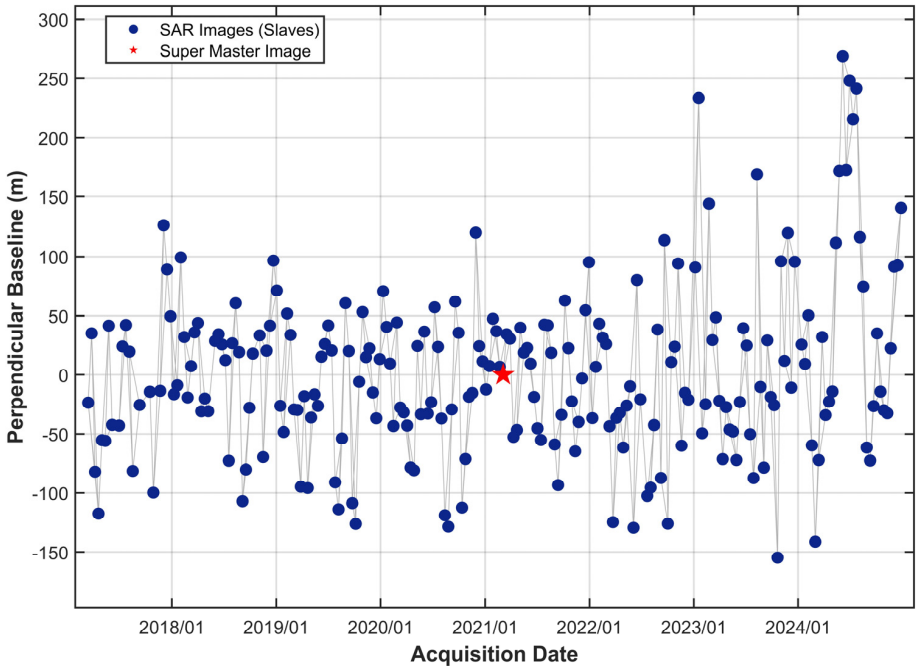

Figure 3. Spatiotemporal baseline configuration of the 231 Sentinel-1A images used in this study. Each line represents an interferometric pair, and the blue pentagram denotes the super-master (reference) image.

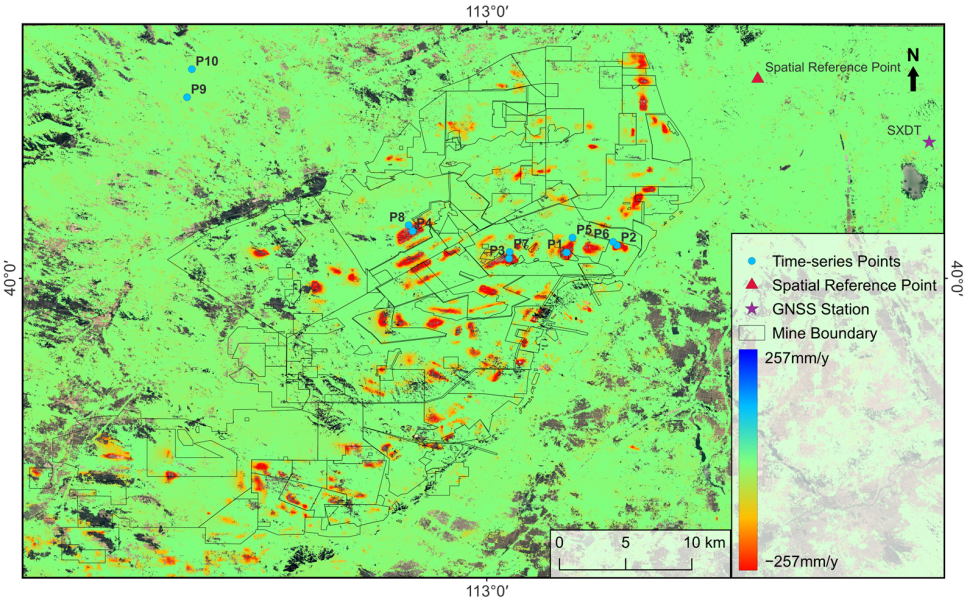

Figure 4. Annual average deformation rate map in the LOS direction of the Datong Coalfield. The red triangle denotes the spatial reference point, assumed to be stable. The blue dots P1–P10 represent representative characteristic points, whose time-series deformation evolution is discussed in Section 5.1.2.

Figure 5 further illustrates the evolution of surface subsidence from localized discrete points to large-scale connectivity across the entire study area. During the initial monitoring phase (2017–2018), deformation was primarily confined to the extraction extent of independent working faces, manifesting as a discrete, point-like distribution. As mining activities progressed from 2019 to 2024, numerous mining areas exhibited a significant trend of expanding and merging subsidence patches. Driven by the sequential extraction of adjacent working faces and the superposition of mining-induced stress, the originally isolated subsidence centers gradually coalesced. This eventually evolved into a large-scale subsidence area characterized by a continuous subsidence gradient, covering an area exceeding 20 km^2. By December 2024, the maximum cumulative subsidence had reached −2085 mm.

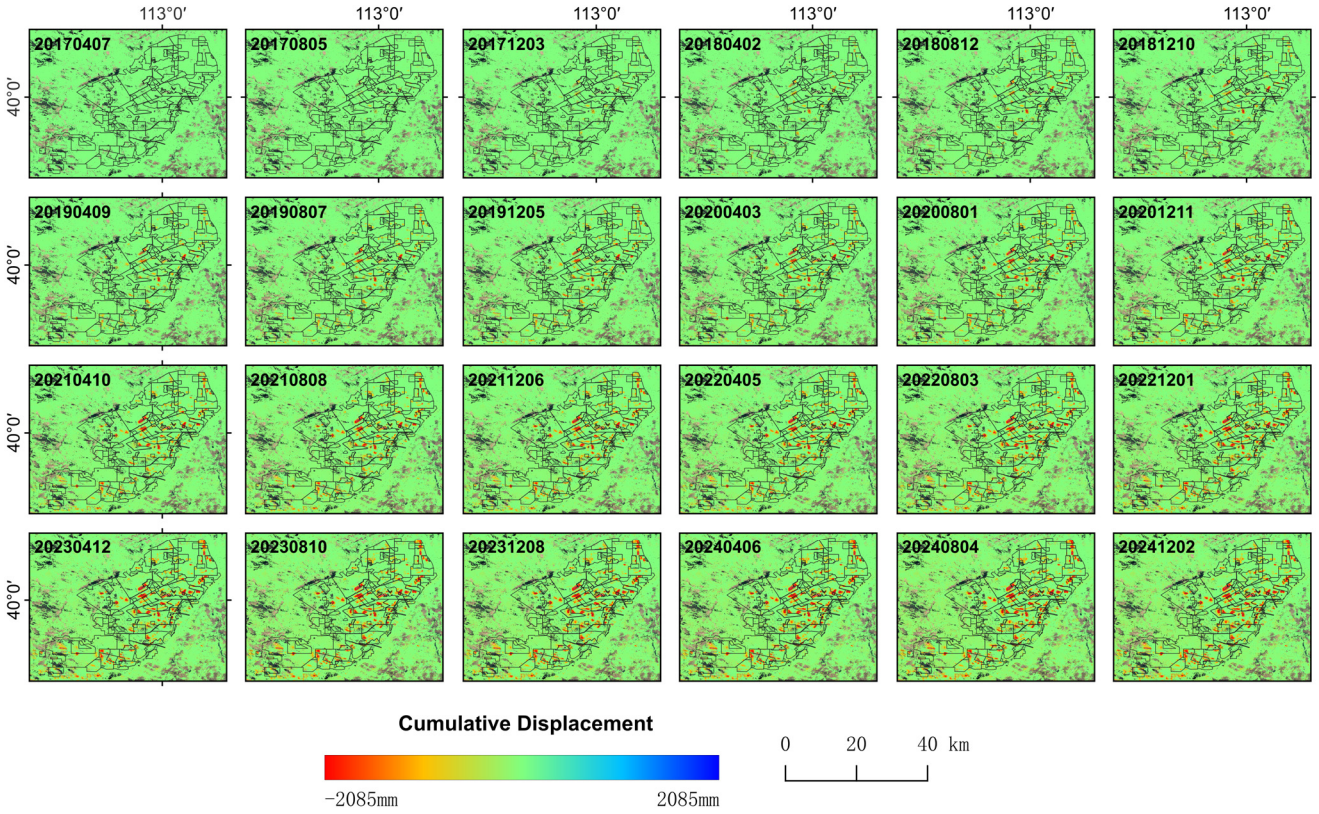

Figure 5. Spatiotemporal evolution characteristics of cumulative surface subsidence in the study area from 2017 to 2024.

4.2. Spatiotemporal Dynamics of Ecological Environmental Quality in the Mining Area

The PCA results confirm the reliability of the MDECI model. Table 2 summarizes the PC1 eigenvalues and contribution rates from 2017 to 2024. The contribution rates range from 60.44% to 75.65%. The average contribution rate reaches 71.19%. These high values indicate that PC1 effectively integrates information from all indicators.

Based on the MDECI model developed in Section 3.2, we obtained the monitoring results for the ecological environmental quality of the study area (Figure 6). The multi-year mean MDECI for the entire Datong Coalfield from 2017 to 2024 was 0.434. In terms of temporal evolution, the ecological quality did not exhibit a continuous linear decline but rather displayed significant oscillatory characteristics, with an overall fitting slope of −0.008/year. Specifically, the MDECI dropped to its lowest point (0.394) in 2018, subsequently recovering to a peak (0.461) in 2021. The ecological low in 2018 was primarily attributed to the extreme high-temperature and drought events in North China that year. Severe moisture stress hindered vegetation growth, a phenomenon confirmed by widespread vegetation browning

observed in Landsat growing-season imagery (see Figure 7) and related literature [40–42]. Despite the dual pressures of climatic fluctuations and mining activities, the regional ecosystem as a whole remained within a range of dynamic equilibrium, demonstrating a certain degree of natural resilience.

Table 2. The eigenvalues and contribution rates of the main components of PCA.

Year	Principal Component Analysis	PC1	PC2	PC3	PC4	PC5
2017	Eigenvalue	0.0714	0.0176	0.0068	0.0038	0.0003
	Percent eigenvalue (%)	71.55	17.66	6.77	3.76	0.26
2018	Eigenvalue	0.0584	0.0266	0.0065	0.0049	0.0002
	Percent eigenvalue (%)	60.44	27.56	6.76	5.03	0.21
2019	Eigenvalue	0.0755	0.0134	0.0070	0.0037	0.0003
	Percent eigenvalue (%)	75.65	13.42	7.00	3.67	0.26
2020	Eigenvalue	0.0702	0.0175	0.0067	0.0055	0.0004
	Percent eigenvalue (%)	70.01	17.42	6.70	5.46	0.41
2021	Eigenvalue	0.0734	0.0172	0.0070	0.0039	0.0003
	Percent eigenvalue (%)	72.08	16.92	6.87	3.88	0.25
2022	Eigenvalue	0.0698	0.0182	0.0064	0.0042	0.0003
	Percent eigenvalue (%)	70.61	18.37	6.47	4.25	0.30
2023	Eigenvalue	0.0710	0.0125	0.0076	0.0031	0.0002
	Percent eigenvalue (%)	75.17	13.27	8.01	3.32	0.23
2024	Eigenvalue	0.0746	0.0155	0.0069	0.0036	0.0002
	Percent eigenvalue (%)	73.98	15.41	6.82	3.58	0.21

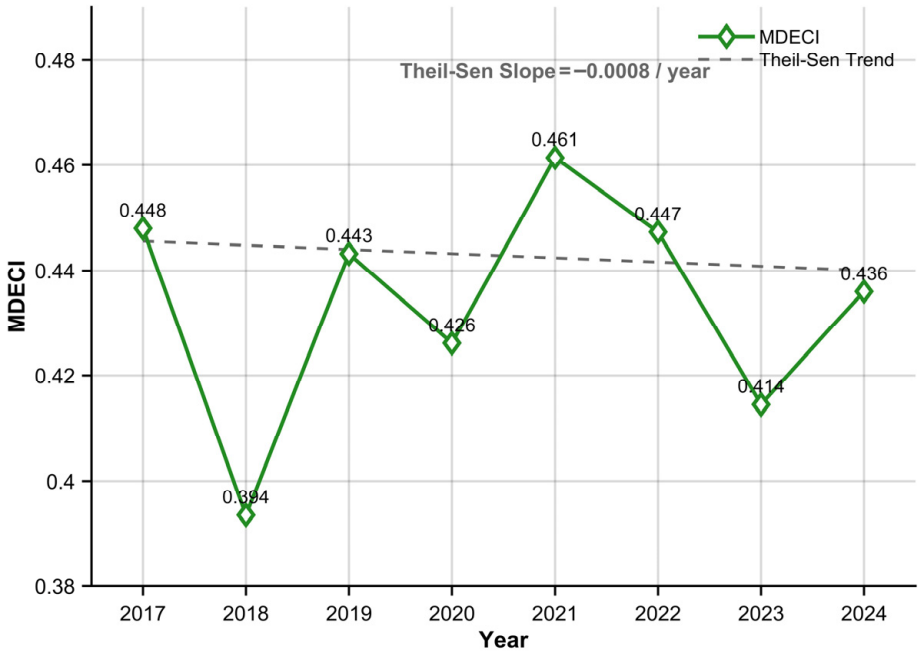

Figure 6. Temporal evolution trend of ecological environmental quality (MDECI) in the Datong Coalfield from 2017 to 2024.

Spatially, the study area exhibited a distinct "core-periphery" differentiation (Figure 8). Low-value areas were primarily concentrated in the mining hinterlands and industrial squares. Influenced by high-intensity surface disturbances, the ecological quality levels in these areas were predominantly categorized as Poor (0–0.20) or Fair (0.20–0.40). In contrast, high-value areas, including Moderate (0.40–0.60), Good (0.60–0.80), and Excellent

(0.80–1.00), were distributed around the periphery of the mining area, forming a natural ecological barrier.

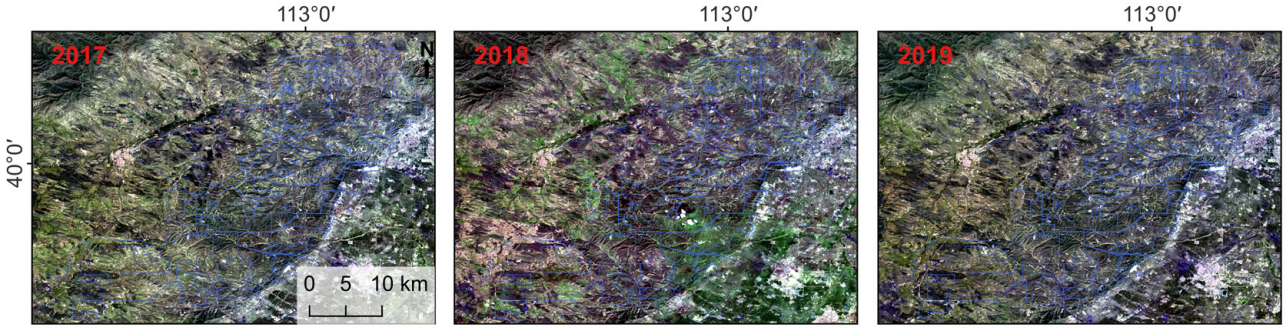

Figure 7. Phenological validation of regional vegetation browning in 2018 based on Landsat true-color imagery.

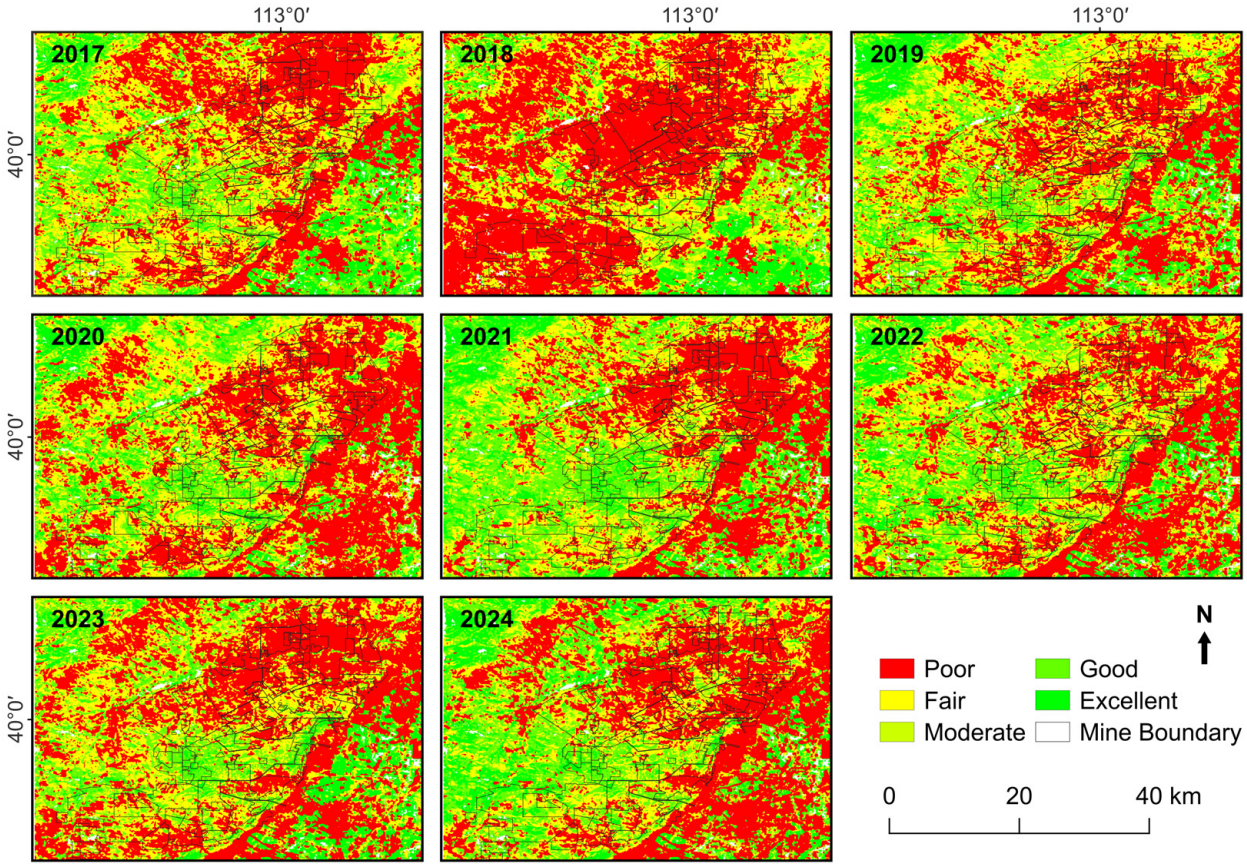

Figure 8. Spatial distribution and evolution of ecological status in the Datong Coalfield (2017–2024).

Furthermore, we conducted continuous monitoring of ecological changes between 2017 and 2024 by calculating the annual MDECI differences (Figure 9). The results indicate that ecological degradation (negative values) and ecological improvement (positive values) exhibit a significant intertwined spatial distribution. Although precise boundary segmentation is difficult at a macroscopic level, the overall trend suggests that areas strongly affected by mining activities generally show a decline in ecological quality, while some subsidence areas and their edges exhibit a clear recovery trend. This spatial pattern of "co-existence of damage and restoration" reflects the dynamic evolution process of the mining environment under the joint influence of continuous mining disturbances and localized ecological recovery.

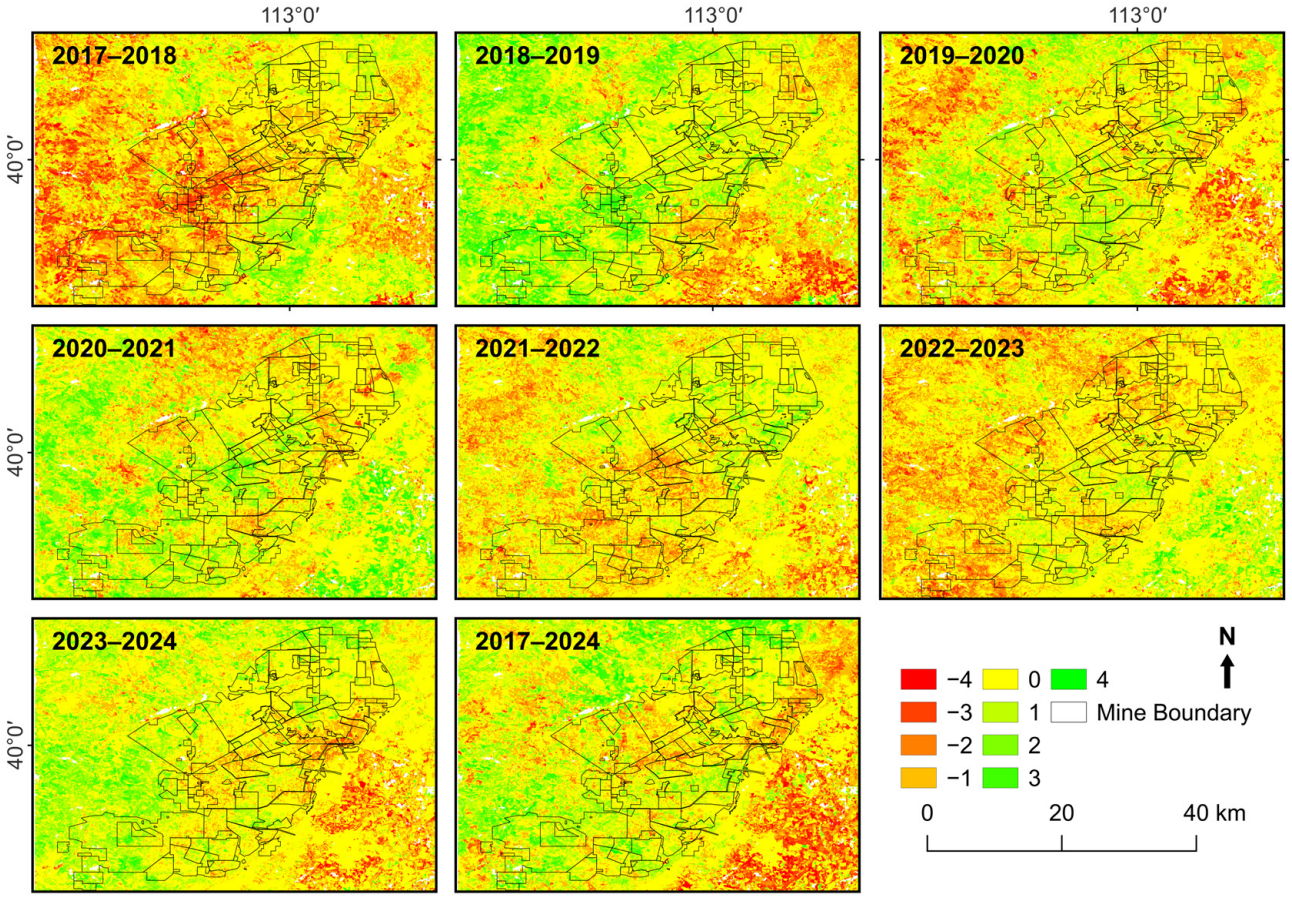

Figure 9. Ecological changes in the Datong Coalfield from 2017 to 2024.

4.3. Non-Linear Response and Spatial Association Between Ecological Quality and Surface Deformation

To deconstruct the relationship between surface deformation and ecological quality, this study applied the gradient-based zonal statistics and bivariate Moran's I methods described in Section 3.3.

4.3.1. Deformation–Ecological Non-Linear Response Mechanism and Turning Point Identification

The response curve derived from the multi-scale gradient zonal statistics (Figure 10) illustrates the variation of MDECI across different subsidence intensities. The results show that the MDECI follows a unimodal non-linear trajectory. In the initial subsidence interval (0 to −100 mm), the mean MDECI increased from 0.371 in the stable zone (>0 mm) to a regional peak of 0.471. This gain aligns with the Intermediate Disturbance Hypothesis (IDH) [36]. The −100 mm mark serves as the ETP, after which the MDECI trajectory shifts from an upward trend to a progressive decline. As cumulative subsidence increases from −100 mm to −1000 mm, the MDECI decreases steadily at a 100 mm sampling scale. In the severe subsidence zone (<−1000 mm), where adaptive intervals of 400 mm were applied to suppress statistical noise arising from sparse pixel samples in extreme deformation areas, the MDECI continued to decrease. The minimum mean value of 0.185 was recorded in the maximum subsidence gradient (<−1800 mm). The details are discussed in Section 5.3.1.

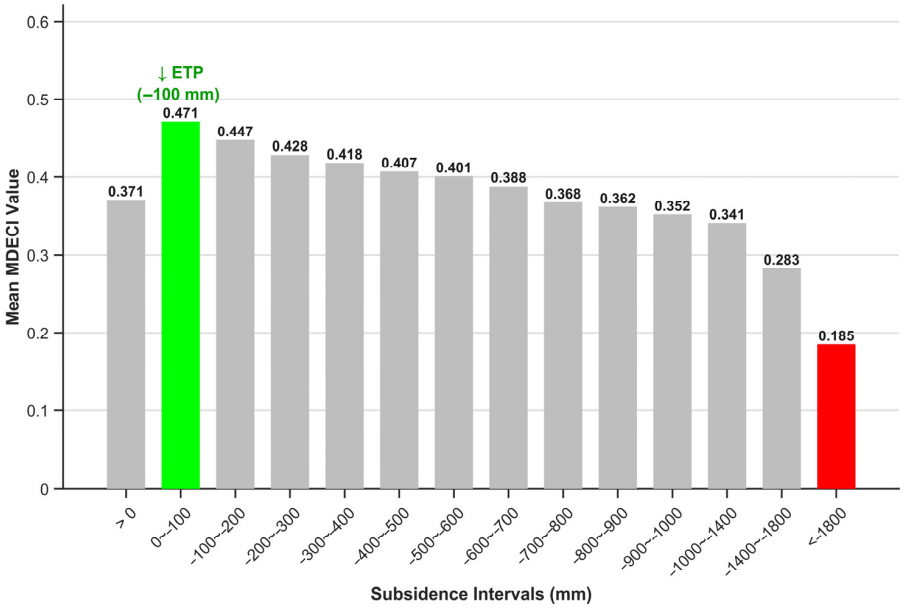

Figure 10. Quantitative relationship and ETP identification between cumulative surface subsidence and MDECI.

4.3.2. Detection of Deformation–Ecological Spatial Association Patterns

To further explore the spatial association between deformation and ecology, this study applied the method described in Section 3.3.2 to generate LISA cluster maps (Figure 11). The results show that 48.88% of the entire area exhibited statistically non-significant spatial associations (Not Significant), while the significantly associated areas intuitively characterized the spatial differentiation between mining-affected and non-mining areas. Specifically, the HL type accounted for 5.09%, manifesting as highly clustered patches in the center of intense mining areas, corresponding to ecologically damaged areas severely affected by mining disturbances. The HH type reached 9.00%, primarily distributed at the edges of subsidence funnels and specific localized regions. This represents high-ecology maintenance areas under a background of intense subsidence, with a coverage scale approximately 1.77 times that of the damaged areas, reflecting the compensatory effects of artificial restoration. Additionally, the LL type (21.94%) and LH type (15.09%) were widely distributed across the periphery of the mining area and unmined regions, constituting the baseline ecological environment unaffected by significant subsidence. Detailed demonstrations are discussed in Section 5.3.2.

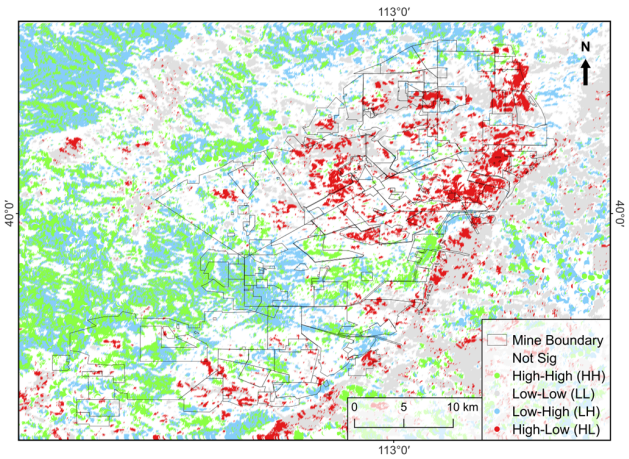

Figure 11. Bivariate LISA cluster map of cumulative subsidence and MDECI in the Datong Coalfield for 2024.

5. Discussion

5.1. Accuracy Validation of Surface Deformation Monitoring and Analysis of Spatiotemporal Evolution Characteristics

5.1.1. GNSS-Based Accuracy Cross-Validation

To ensure the reliability of the surface deformation monitoring results presented in Section 4.1, continuous GNSS observation data from the SXDT station within the study area were utilized to validate the InSAR deformation results (marked in Figure 1 with a purple pentagram). The three-dimensional GNSS displacement components were projected into the radar LOS direction according to Equation (8). The time-series comparison results (Figure 12) demonstrate high consistency in deformation trends between the two datasets. Quantitative statistics indicate that the STD of the difference between InSAR and GNSS monitoring results is 5.58 mm, with a RMSE of 8.79 mm. This level of accuracy validates the reliability of the SBAS-InSAR technique for long-term subsidence monitoring in the study area, providing precise deformation constraint information for subsequent ecological response analysis.

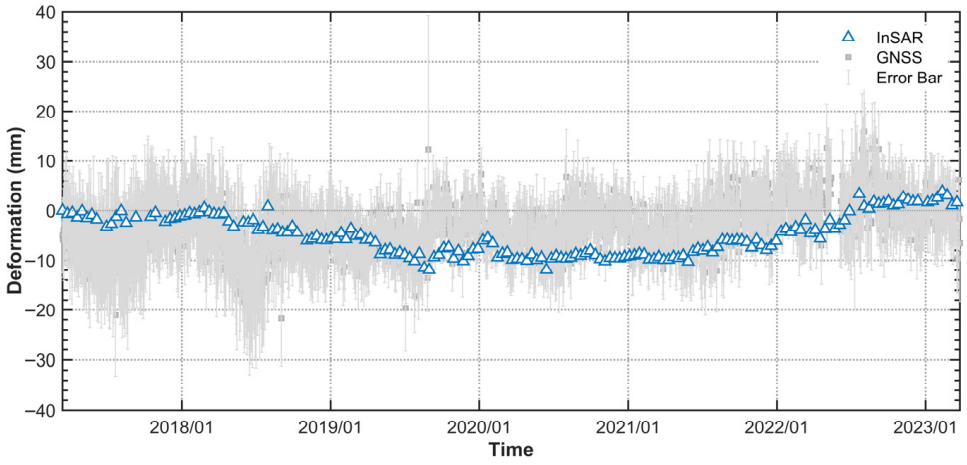

Figure 12. Time-series comparison of LOS deformation between InSAR monitoring results and GNSS-measured data.

5.1.2. Spatiotemporal Evolution Patterns and Typical Deformation Modes

To resolve the spatial heterogeneity of surface deformation described in Section 4.1, this study examines the evolution from two dimensions: the spatial progression process and typical temporal response modes.

Regarding spatial evolution, taking the Jinhuagong mining area (Figure 13) as an example, multiple localized subsidence centers within the study area continuously expanded and underwent spatial coupling, evolving into a large-scale subsidence area with a continuous subsidence gradient. In 2017–2018, deformation was primarily characterized by localized subsidence centers confined to the extraction extent of single working faces. During this stage, the disturbance ranges of various mining sectors were relatively independent, with no large-scale connectivity formed spatially. From 2019 to 2021, as underground mining progressed, the influence ranges of adjacent working faces began to overlap. Driven by the stress superposition effect, originally isolated subsidence centers expanded and coalesced. Finally, during 2022–2024, the deformation field culminated in an extensive subsidence area with a continuous gradient. This progression indicates that large-scale subsidence areas in the study area are not instantaneous formations but are the result of the non-linear spatiotemporal accumulation and superposition of multiple independent mining units.

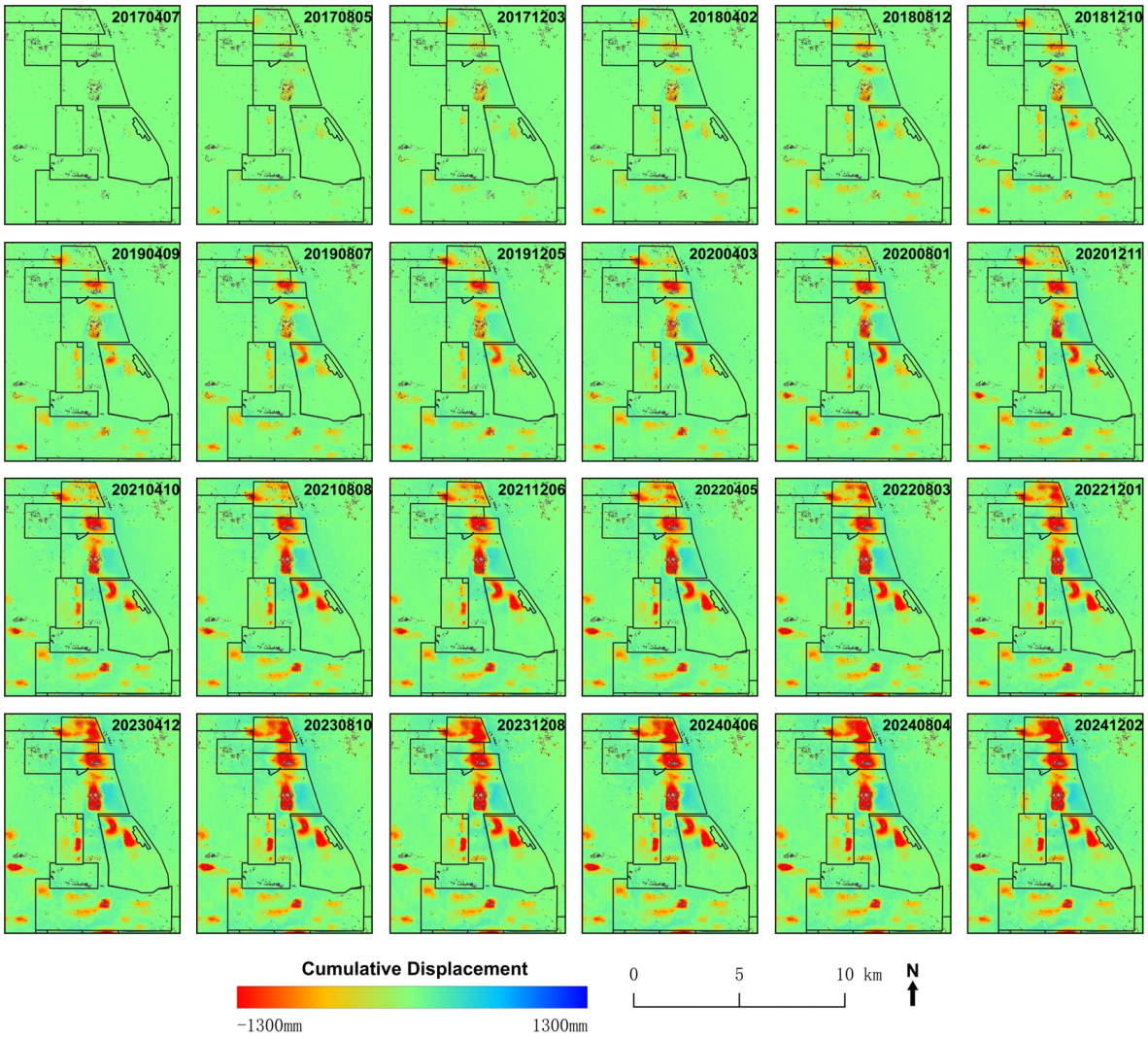

Figure 13. Spatiotemporal evolution trajectory of cumulative surface deformation in the Jinhuagong mining area (2017–2024).

Regarding temporal response modes, to capture the nuances of deformation evolution under varying mining intensities, ten characteristic points (P1–P10, indicated by blue dots in Figure 4) were selected for long-term time-series tracking. Figure 14 presents the cumulative subsidence curves of these points, which exhibit three distinct non-linear response patterns. The first category represents continuous and intense subsidence, most prominently observed at points P1–P4 located in the center of the goaf. Specifically, P1, situated at the core of the primary subsidence funnel, showed a near-linear and persistent increase in cumulative subsidence, with the maximum LOS value exceeding −2000 mm by the end of 2024, while P2, P3, and P4 also surpassed −1500 mm. The second category comprises stepped and sudden activation patterns, where P5, P6, and P8 illustrate the staged characteristics of mining-induced subsidence. For instance, after an initial rapid descent, the curve for P5 flattened from 2019 onwards and stabilized at approximately −600 mm, reflecting the gradual attainment of a new mechanical equilibrium post-mining. Conversely, P7 revealed a lagged activation phenomenon in adjacent areas. It remained relatively stable until May 2023 (with a cumulative deformation of −189.0 mm) but subsequently underwent an active subsidence phase. The cumulative deformation reached −605.5 mm by June 2024, representing a net increment of 416.5 mm within this period. This process spanned approximately 12.4 months (corresponding to 31 consecutive SAR

observations), signaling the initiation of a new working face or the reactivation of nearby legacy goafs. The third category represents stability in non-mining areas, as exemplified by P9 and P10, which were selected far from the goafs and exhibited only minor fluctuations around the 0 mm baseline throughout the 8-year monitoring period without trend-based deformation, highlighting the geological stability of the mining area's periphery.

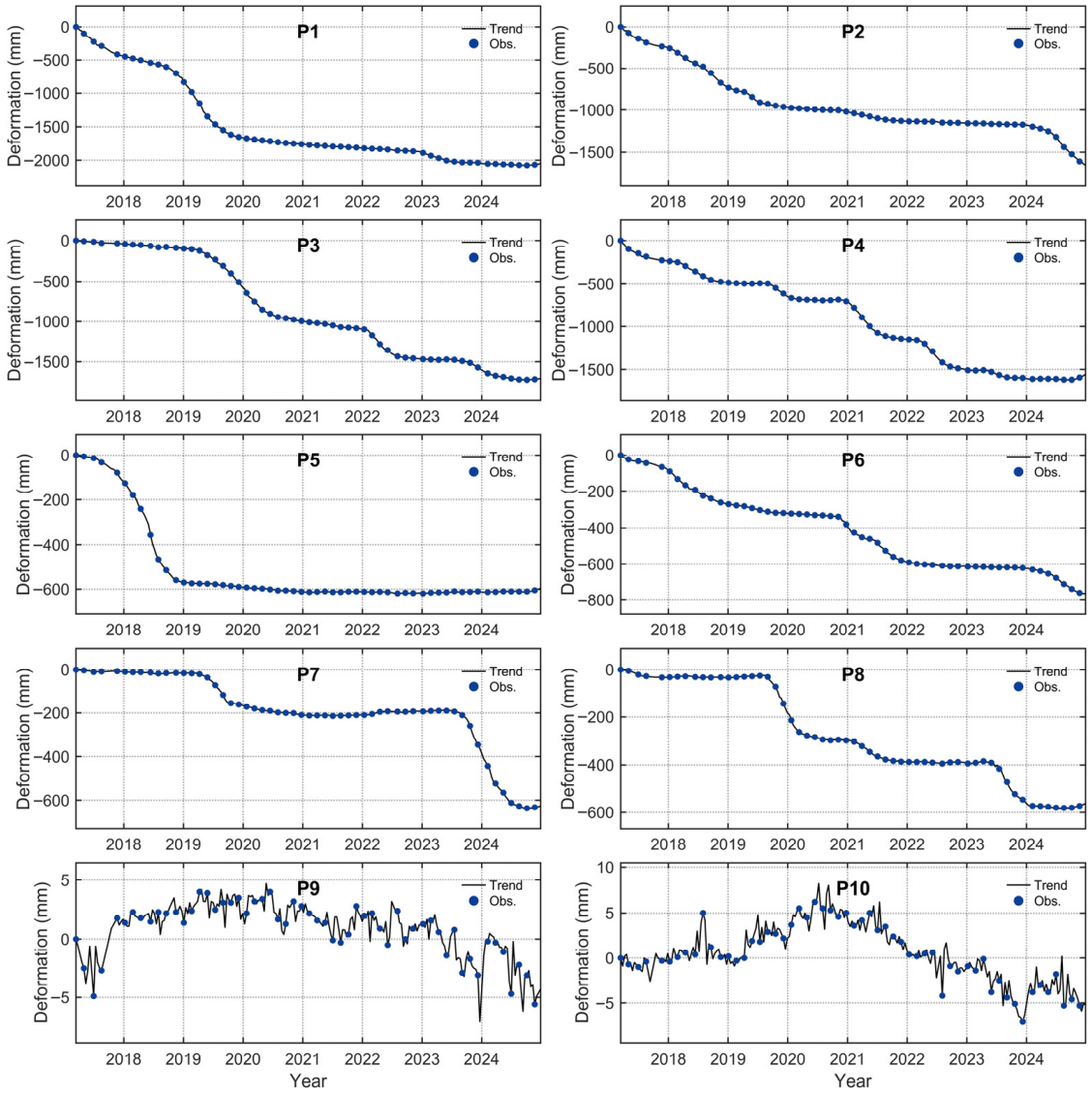

Figure 14. Deformation time series of characteristic points representing typical deformation modes in the mining area.

5.2. MDECI Model Performance Evaluation

The credibility of the spatiotemporal evolution trajectory revealed in Section 4.2 fundamentally depends on the methodological framework and robustness of the evaluation model itself. To verify the performance of the MDECI model in the mining area, this study conducts an assessment from two dimensions—comprehensive performance validation and internal consistency and coordination—following the method described in Section 3.4.2.

5.2.1. Comprehensive Performance Validation of MDECI

The comprehensive performance of MDECI was validated by comparing it with existing established models, namely RSEI [32] and Mine-specific Eco-environment Index (MSEEI) [7] (Figure 15). Cross-correlation analysis shows that the correlation coefficient

between MDECI and the traditional RSEI reached 0.906, ensuring continuity in evaluation standards. Meanwhile, its correlation with MSEEI was even higher (0.931), confirming the superior adaptability of the new model to complex surface features in mining areas. Analysis of the annual component integration efficacy (Figure 16) indicates that while maintaining high sensitivity to natural ecological factors, such as greenness and wetness, MDECI effectively captures structural variations induced by deformation.

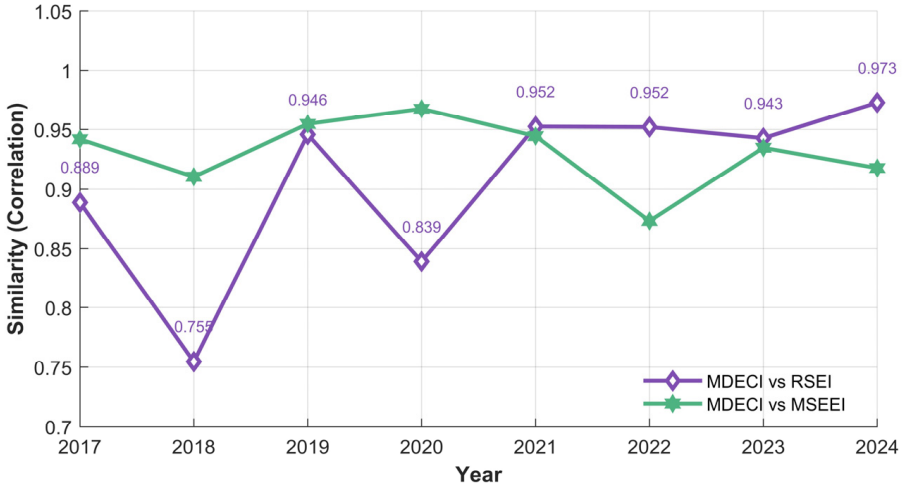

Figure 15. Cross-correlation analysis between MDECI and existing established models (RSEI and MSEEI).

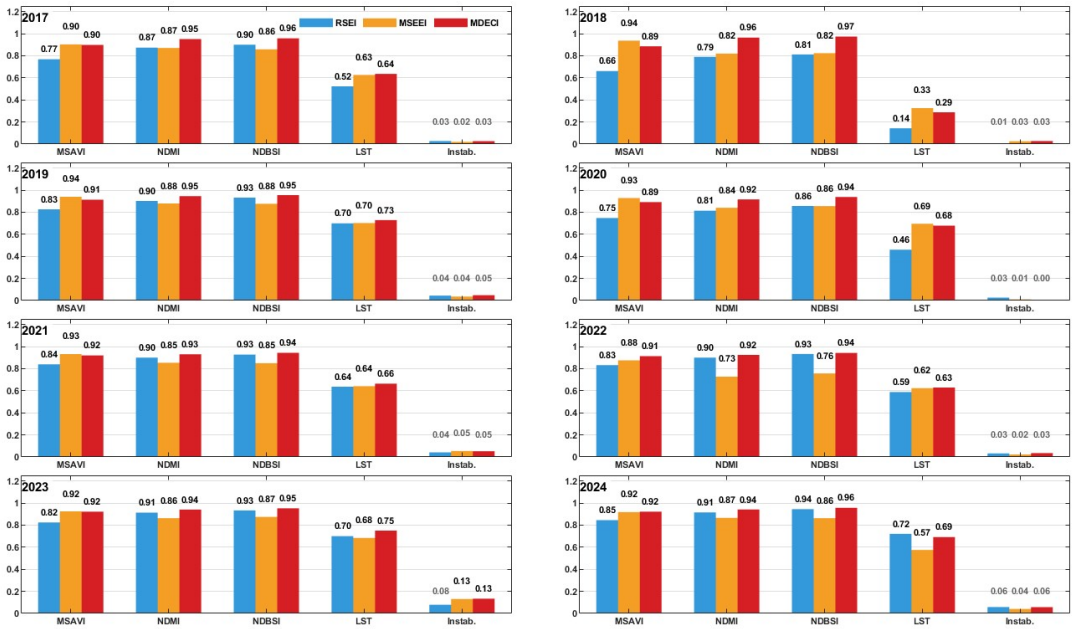

Figure 16. Temporal evolution trends in the representativeness of ecological indices and analysis of their component integration efficacy.

The temporal evolution of the ACC (Figure 17) further reveals differences in model representativeness. The ACC values for MDECI remained at the highest level (0.63–0.75) throughout the 2017–2024 period, indicating its robust capability to integrate multi-dimensional information. Notably, under the extreme drought stress of 2018, the representativeness of the traditional RSEI significantly declined due to background noise interference (ACC = 0.482), demonstrating its susceptibility to failure under extreme meteorological conditions. In contrast, MDECI maintained a high ACC value of 0.628 through

its adaptive weight adjustment mechanism. This significant "environmental resilience" proves that MDECI can effectively isolate interference from non-mining disturbance factors, providing a more robust basis for long-term monitoring in mining areas.

In summary, MDECI is positioned as an optimized model that combines the universality of RSEI with the adaptability of MSEEI. Building on the classical model's ability to control macro-ecological processes—specifically the "water-heat-vegetation" nexus—it achieves precise quantitative characterization of geological damage in mining areas by introducing deformation constraints. However, certain application boundaries remain. On the one hand, the evaluation accuracy of MDECI depends to some extent on the stability of InSAR deformation retrieval. In areas with fragmented terrain or extremely high vegetation cover leading to severe SAR decorrelation, obtaining deformation constraint terms may be restricted. On the other hand, compared to traditional optical indices, the processing workflow of MDECI is more complex, requiring higher precision in data pre-processing. Therefore, further integrating multi-source deformation monitoring methods to enhance the model's generalization capability in severe decorrelation areas will be a key optimization direction for improving the applicability of this index in future research.

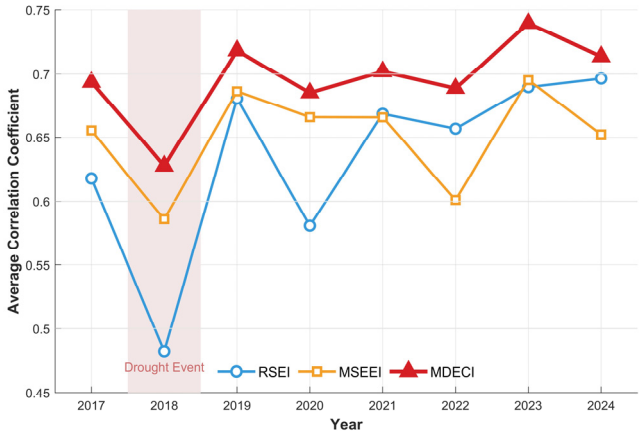

Figure 17. Comparison of the ACC among MDECI, RSEI, and MSEEI.

5.2.2. Consistency Analysis of Internal Driving Mechanisms

The principal component loadings intuitively reflect the contribution weights and impact directions of various indicators on ecological quality. The monitoring results (Figure 18) reveal a clear "Optical Dominance-Deformation Constraint" hierarchical mechanism within the MDECI model. Optical indicators exhibited high-magnitude loadings ($|\text{Loadings}| > 0.4$), constituting the foundational framework of the ecological assessment. Specifically, MSAVI and NDMI consistently maintained high positive loadings between 0.5 and 0.6, indicating that they exert a positive influence on the ecological environment of the mining area. Conversely, NDBSI remained stable at approximately -0.5, serving as a primary negative factor. Although LST generally showed negative loadings, it exhibited significant fluctuations in 2018, with the absolute loading value decreasing to approximately -0.2. This aligns with the extreme drought events of that year, reflecting a temporary attenuation (blunting) of LST sensitivity towards ecological quality under extreme high-temperature stress. Unlike the optical indicators, the loadings of the newly introduced Instability indicator fluctuated between 0 and -0.05, consistently remaining negative. The consistent negative loading confirms that surface Instability acts as a significant deformation constraint highly coupled with the mining-induced degradation process. Rather than a secondary factor, surface deformation serves as a fundamental structural constraint that is closely associated with ecological decline.

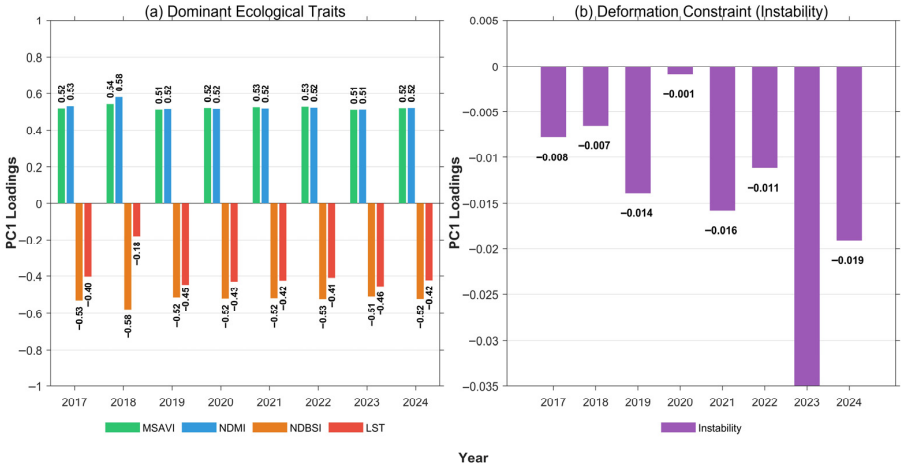

Figure 18. Interannual evolution of the PC1 loading vectors in the MDECI model (2017–2024): (**a**) Dominant ecological traits, where optical indicators (MSAVI, NDMI, NDBSI, and LST) exhibit high-magnitude contributions to ecological quality. (**b**) The Instability indicator, acting as a localized deformation constraint with persistent negative loadings that reflect the structural restrictive effect of surface deformation.

5.3. Non-Linear Response Mechanisms and Spatial Pattern Analysis

The "unimodal" response curve and spatial clustering patterns demonstrated in Section 4.3 confirm that the driving influence of surface deformation on the ecosystem is not a simple linear negative correlation. This study analyzes the interaction between surface deformation and ecological quality from two dimensions: mining-induced deformation disturbance and localized ecological restoration.

5.3.1. "Unimodal" Characteristics of Ecological Damage and Turning Point Analysis

The response curve in Figure 10 confirms that the impact of subsidence on ecological quality follows a unimodal (single-peak) pattern rather than a simple linear decline. This reflects the dynamic competition between mining-induced disturbance and the ecosystem's self-regulatory capacity. In the initial subsidence stage (0 to −100 mm), the observed "ecological gain"—where the MDECI rises from 0.371 to 0.471—points to the ecosystem's early-stage resilience. Within this subtle deformation range, the slight alteration of micro-topography may facilitate localized ecological optimization. During this phase, the positive response to micro-geomorphological adjustments outweighs the initial deformation stress on vegetation. However, the −100 mm mark represents the ETP [36] where this balance shifts. Beyond this point, the MDECI begins a progressive decline. This suggests that as subsidence exceeds the critical threshold, ground fissures and soil structure disruption start to dominate the ecological response. Unlike a sudden "collapse" at a specific depth, the degradation observed here is progressive, indicating that the cumulative impact of deformation steadily erodes the ecosystem's self-maintenance capability. Notably, by employing a multi-scale binning strategy, the response curve provides a robust representation of the degradation trajectory in the severe subsidence zone (<−1000 mm). The adaptive intervals effectively suppress localized statistical noise, revealing a consistent downward trend. In the extreme subsidence zones (exceeding −1800 mm), the cumulative surface damage ultimately leads to a significant loss of ecological integrity, with MDECI values reaching the minimum level of 0.185.

5.3.2. Spatial Heterogeneity of Mining Damage and Ecological Restoration

To reveal the distinct structural disturbances and ecological spatial association patterns under various clustering modes, a spatial overlay analysis was conducted (Figure 19).

This integrated the LISA clustering results (Figure 11) with the surface deformation field, MDECI, and Red-Green-Blue (RGB) imagery. The HL mode (accounting for 5.09%) coincides closely with the centers of the subsidence funnels within the deformation field (see Figure 19a). Spatial overlaying demonstrates that in areas with intense subsidence rates (represented by red patches), the MDECI simultaneously exhibits significantly low values. This negative correlation between surface deformation and ecological quality indicates that surface damage caused by large-scale underground mining imposes a structural constraint on the ecosystem. Severe surface deformation alters the habitat conditions, leading to observable ecological degradation associated with geomechanical stress. Conversely, the HH mode (9.00%) is situated within heavy subsidence areas, yet the MDECI maintains a high level (see Figure 19b). Although the RGB imagery is limited by resolution in identifying micro-features, the multi-source data comparison highlights these "high ecological maintenance areas" under intense subsidence, where severe ground sinking has not resulted in synchronous ecological degradation. Based on the actual governance context of the Datong Coalfield, this reflects the ecological compensation effects generated by land reclamation plans and artificial vegetation restoration programs, which effectively offset the negative impacts of surface deformation [43]. The LH mode (15.09%) is primarily distributed in undisturbed original forest and grassland areas. These areas exhibit high surface stability and excellent ecological quality, constituting a natural ecological barrier for the mining area (see Figure 19c). In contrast, the LL mode (21.94%) represents areas where the surface is relatively stable but ecological quality is limited (see Figure 19d). Considering the topographical distribution, this is primarily restricted by the natural habitat and poor soil conditions of the Datong Coalfield's surroundings, rather than being associated with mining activities. In summary, the ecological evolution of the Datong Coalfield presents a complex landscape where ecological damage and local high-level maintenance coexist. Introducing the Instability indicator as a deformation constraint into the evaluation framework allows for a more scientific isolation of mining-induced impacts, providing a robust basis for differentiated ecological restoration strategies.

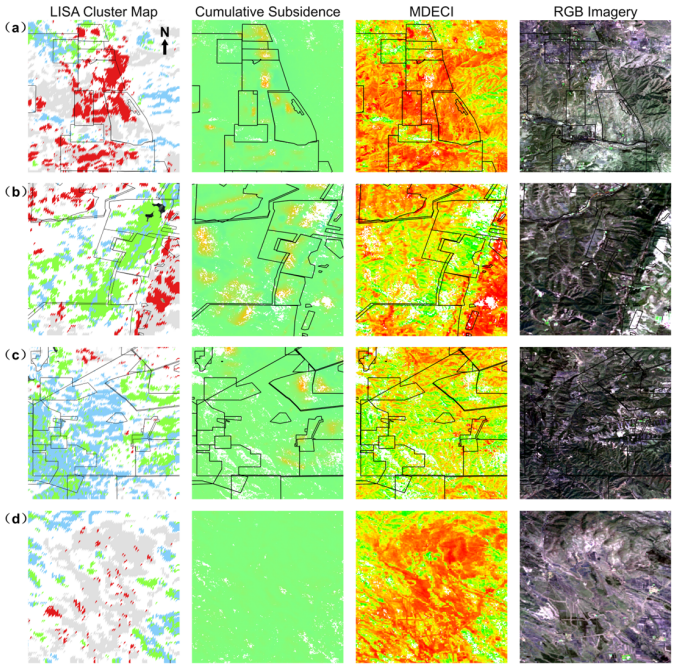

Figure 19. Multi-dimensional analysis of the microscopic mechanisms underlying the spatial coupling patterns between surface deformation and ecological quality: (**a**) HL type, (**b**) HH type, (**c**) LH type, (**d**) LL type.

6. Conclusions

This study first processed 231 Sentinel-1 images from 2017 to 2024 using SBAS-InSAR technology to obtain high-precision surface deformation time series. The annual deformation increments were then transformed into a surface Instability indicator, which was integrated with multispectral ecological indices via PCA to construct the MDECI model. Finally, the non-linear response mechanisms, ETP, and spatial clustering characteristics between surface deformation and ecological quality were deeply analyzed. The main conclusions are as follows:

(1) Revelation of spatiotemporal evolution patterns in surface subsidence and ecological degradation. SBAS-InSAR illustrated that multiple localized subsidence centers within the study area continuously expanded and underwent spatial coupling, evolving into a large-scale subsidence area with a continuous subsidence gradient and a maximum cumulative subsidence of −2085 mm. Driven by this intense deformation disturbance, the mean ecological quality index in the core subsidence areas dropped to 0.185, significantly lower than the regional average of 0.434.

(2) Validation of the superiority and robustness of the MDECI model in complex monitoring environments. Performance evaluation showed that the ACC (0.63–0.75) of MDECI consistently remained at the highest level. Notably, during the extreme drought of 2018, MDECI successfully overcame the representativeness failure of the traditional RSEI (where ACC dropped sharply to 0.482) by maintaining a reliable level of 0.628. This demonstrates the critical role of surface stability indicators in isolating background noise and enhancing assessment accuracy in mining areas.

(3) Identification of the non-linear "unimodal" response mechanism and the ETP. A significant unimodal relationship was observed between cumulative subsidence and MDECI, with −100 mm identified as the ETP. In the initial subsidence stage (0 to −100 mm), a localized gain was observed, where the MDECI increased from 0.371 to a peak of 0.471. Beyond this critical turning point, the ecosystem transitions into a stage of progressive decline, with the MDECI ultimately decreasing to 0.185 in severe subsidence zones. This quantitative characterization of the non-linear response provides an objective basis for assessing ecological resilience and identifying turning point in mining areas.

(4) Analysis of the spatial distribution of ecological damage (HL type, 5.09%) and high-ecology maintenance (HH type, 9.00%). Results indicate that the scale of the HH areas is 1.77 times that of the HL-type damaged areas, confirming that intense surface sinking does not inevitably trigger synchronized ecological degradation. This quantitatively reflects the compensatory effects generated by ecological reclamation plans and vegetation restoration projects, enabling the region to maintain ecological quality against the trend of severe deformation disturbances.

Author Contributions: Conceptualization, B.Z. and L.Z.; methodology, B.Z. and L.Z.; software, L.Z.; validation, L.Z., H.X., Y.L. and H.Z.; formal analysis, L.Z.; investigation, L.Z., B.Z. and H.X.; resources, B.Z.; data curation, L.Z. and Z.Z.; writing—original draft preparation, L.Z.; writing—review and editing, L.Z., B.Z., Q.S. and Z.Z.; visualization, L.Z.; supervision, B.Z. and Q.S.; project administration, B.Z.; funding acquisition, B.Z., Y.L. and H.Z. All authors have read and agreed to the published version of the manuscript.

Funding: This research was funded by the Key Laboratory of Ionic Rare Earth Resources and Environment, Ministry of Natural Resources of the People's Republic of China (No. 2024IRERE403), the Natural Science Foundation of Shanxi Province (Grant No. 202403021211007), and the Engineering Technology Innovation Center for Ecological Protection and Restoration in the Middle Yellow River, Ministry of Natural Resources (No. 2025069).

Data Availability Statement: Sentinel-1A SAR images are available through the Alaska Satellite Facility Vertex website (ASF; https://search.asf.alaska.edu/; accessed on 26 October 2025); Landsat 8 and 9 OLI/TIRS images are available through the U.S. Geological Survey website (USGS; https://earthexplorer.usgs.gov/; accessed on 30 October 2025); Sentinel-1 Precise Orbit Determination (POD) auxiliary data (POEORB) are available at the ESA STEP auxiliary data server (http://step.esa.int/auxdata/orbits/Sentinel-1/POEORB/S1A/; accessed on 26 October 2025); SRTM Digital Elevation Model (DEM) data are available at the U.S. Geological Survey website (USGS; http://earthexplorer.usgs.gov/; accessed on 26 October 2025); GNSS monitoring data are available at the Earthquake Data Service Center (EQDSC; https://data.earthquake.cn/index.html; accessed on 26 October 2025); administrative boundaries are available at the Resource and Environment Science and Data Center (RESDC; https://www.resdc.cn/; accessed on 26 October 2025).

Conflicts of Interest: The authors declare no conflicts of interest.

Appendix A

Table A1. Mathematical formulations and descriptions of the foundational spectral indicators used in MDECI.

Indicator	Full Name	Formula	Source
MSAVI	Modified Soil Adjusted Vegetation Index	$\frac{2\times\rho_{NIR}+1-\sqrt{(2\times\rho_{NIR}+1)^2-8\times(\rho_{NIR}-\rho_{Red})}}{2}$ where ρ_{NIR} and ρ_{Red} represent the near-infrared (NIR) and red bands of the Landsat 8 OLI/TIRS and Landsat 9 OLI-2/TIRS-2 Level-2 products, respectively.	[44]
NDMI	Normalized Difference Moisture Index	$\frac{\rho_{NIR}-\rho_{SWIR1}}{\rho_{NIR}+\rho_{SWIR1}}$ where ρ_{NIR} and ρ_{SWIR1} represent the near-infrared (NIR) and short-wave infrared 1 (SWIR1) bands of the Landsat 8 OLI/TIRS and Landsat 9 OLI-2/TIRS-2 Level-2 products, respectively.	[45]
NDBSI	Normalized Difference Built-up and Soil Index	$(SI+IBI)/2$ where $SI=\frac{(\rho_{SWIR1}+\rho_{Red})-(\rho_{Blue}+\rho_{NIR})}{(\rho_{SWIR1}+\rho_{Red})+(\rho_{Blue}+\rho_{NIR})}$ $IBI=\frac{2\rho_{SWIR1}/(\rho_{SWIR1}+\rho_{NIR})-(\rho_{NIR}/(\rho_{NIR}+\rho_{Red})+\rho_{Green}/(\rho_{Green}+\rho_{SWIR1}))}{2\rho_{SWIR1}/(\rho_{SWIR1}+\rho_{NIR})+(\rho_{NIR}/(\rho_{NIR}+\rho_{Red})+\rho_{Green}/(\rho_{Green}+\rho_{SWIR1}))}$ where ρ_{Red}, ρ_{Green}, ρ_{Blue}, ρ_{NIR}, and ρ_{SWIR1} represent the red, green, blue, near-infrared, and short-wave infrared 1 bands of the Landsat 8 OLI/TIRS and Landsat 9 OLI-2/TIRS-2 Level-2 products, respectively.	[33,46,47]
LST	Land Surface Temperature	$LST=T/[1+(\lambda_1 T/\rho)ln\varepsilon]$ where $T=K_2/ln(K_1/L+1)$ $L=gain\times DN+bias$ where DN represents the digital number of the pixel, $gain$ and $bias$ are the gain and offset coefficients of the band, respectively, K_1 and K_2 are the sensor calibration constants, λ_1 is the central wavelength of the thermal infrared band, ε denotes the land surface emissivity, and $\rho=0.01438\ m\cdot K$.	[48,49]

References

1. Jing, Z.; Wang, J.; Zhu, Y.; Feng, Y. Effects of land subsidence resulted from coal mining on soil nutrient distributions in a loess area of China. *J. Clean. Prod.* **2018**, *177*, 350–361. [CrossRef]
2. Yang, X.; Bai, X.; Yao, W.; Li, P.; Hu, J.; Kang, L. Spatio-Temporal Dynamics and Driving Forces of Soil Organic Carbon Changes in an Arid Coal Mining Area of China Investigated Based on Remote Sensing Techniques. *Ecol. Indic.* **2024**, *158*, 111453. [CrossRef]
3. Song, D.; Hu, Z.; Yu, Y.; Zhang, F.; Sun, H. Assessing ecological impacts and recovery in coal mining areas: A remote sensing and field data analysis in Northwest China. *Remote Sens.* **2024**, *16*, 2236. [CrossRef]
4. Yan, W.; Chen, Z.; Chen, J.; Zhao, C. Spatiotemporal Patterns of Vegetation Evolution in a Deep Coal Mining Subsidence Area: A Remote Sensing Study of Liangbei, China. *Remote Sens.* **2024**, *16*, 3204. [CrossRef]
5. Tang, F.; Ma, T.; Tang, J.; Yang, Q.; Xue, J.; Zhu, C.; Wang, C. Space-time dynamics and potential drivers of soil moisture and soil nutrients variation in a coal mining area of semi-arid China. *Ecol. Indic.* **2023**, *157*, 111242. [CrossRef]
6. Xu, H.; Wang, Y.; Guan, H.; Shi, T.; Hu, X. Detecting ecological changes with a remote sensing based ecological index (RSEI) time series and change vector analysis. *Remote Sens.* **2019**, *11*, 2345.
7. Zhang, P.; Chen, X.; Ren, Y.; Lu, S.; Song, D.; Wang, Y. A novel mine-specific eco-environment index (MSEEI) for mine ecological environment monitoring using Landsat imagery. *Remote Sens.* **2023**, *15*, 933. [CrossRef]

8. Chen, Y.; Suo, Z.; Lu, H.; Cheng, H.; Li, Q. Active-Passive remote sensing evaluation of ecological environment quality in Juye mining area, China. *Remote Sens.* **2023**, *15*, 5750. [CrossRef]
9. Yang, L.; Shi, L.; Li, J.; Kong, H.; Hua, D. Analysis of spatiotemporal changes and driving forces of ecological environment quality in Northwest China mining area. *Sci. Rep.* **2025**, *15*, 21273. [CrossRef]
10. Yang, X.; Meng, F.; Fu, P.; Zhang, J.; Liu, Y. Instability of the remote sensing ecological index and its optimisation for time frequency and scale. *Ecol. Inform.* **2022**, *72*, 101870. [CrossRef]
11. Zhu, Z.; Cao, H.; Yang, J.; Shang, H.; Ma, J. Ecological environment quality assessment and spatial autocorrelation of northern Shaanxi mining area in China based-on improved remote sensing ecological index. *Front. Environ. Sci.* **2024**, *12*, 1325516. [CrossRef]
12. Berardino, P.; Fornaro, G.; Lanari, R.; Sansosti, E. A new algorithm for surface deformation monitoring based on small baseline differential SAR interferometry. *IEEE Trans. Geosci. Remote Sens.* **2002**, *40*, 2375–2383.
13. Ma, D.; Zhao, S. Quantitative analysis of land subsidence and its effect on vegetation in Xishan coalfield of Shanxi Province. *ISPRS Int. J. Geo-Inf.* **2022**, *11*, 154.
14. Zhang, B.; Chang, L.; Stein, A. Spatio-temporal linking of multiple SAR satellite data from medium- and high-resolution RADARSAT-2 images. *ISPRS J. Photogramm. Remote Sens.* **2021**, *176*, 222–236.
15. Zhang, B.; Chang, L.; Stein, A. A model-backfeed deformation estimation method for revealing 20-year surface dynamics of the Groningen gas field using multi-platform SAR imagery. *Int. J. Appl. Earth Obs. Geoinf.* **2022**, *111*, 102847.
16. Zhang, B.; Chang, L.; Wang, Z.; Wang, L.; Ye, Q.; Ye, Q.; Stein, A. Multi-decadal Dutch coastal dynamic mapping with multi-source remote sensing imagery. *Int. J. Appl. Earth Obs. Geoinf.* **2025**, *138*, 104452.
17. Ma, B.; Gao, R.; Che, D.; Xu, Z.; Wang, D.; Sun, Y. Multisource remote sensing monitoring and analyzing for land subsidence and crop growth in a coal mining area under different rainfall conditions. *Environ. Dev.* **2024**, *52*, 101086. [CrossRef]
18. Duo, L.; Wang, J.; Zhong, Y.; Jiang, C.; Chen, Y.; Guo, X. Ecological environment quality assessment of coal mining cities based on GEE platform: A case study of Shuozhou, China. *Int. J. Coal Sci. Technol.* **2024**, *11*, 75. [CrossRef]
19. Xu, Y.; Li, T.; Tang, X.; Zhang, X.; Fan, H.; Wang, Y. Research on the Applicability of DInSAR, Stacking-InSAR and SBAS-InSAR for Mining Region Subsidence Detection in the Datong Coalfield. *Remote Sens.* **2022**, *14*, 3314. [CrossRef]
20. Nie, X.; Hu, Z.; Ruan, M.; Zhu, Q.; Sun, H. Remote-Sensing Evaluation and Temporal and Spatial Change Detection of Ecological Environment Quality in Coal-Mining Areas. *Remote Sens.* **2022**, *14*, 345. [CrossRef]
21. Bi, Y.; Zhang, J.; Song, Z.; Wang, Z.; Qiu, L.; Hu, J.; Gong, Y. Arbuscular mycorrhizal fungi alleviate root damage stress induced by simulated coal mining subsidence ground fissures. *Sci. Total Environ.* **2019**, *652*, 398–405. [CrossRef] [PubMed]
22. Wang, J.; Wang, P.; Qin, Q.; Wang, H. The effects of land subsidence and rehabilitation on soil hydraulic properties in a coal mining area of the Loess Plateau, China. *Environ. Earth Sci.* **2017**, *76*, 195.
23. Torres, R.; Snoeij, P.; Geudtner, D.; Bibby, D.; Davidson, M.; Attema, E.; Potin, P.; Rommen, B.; Floury, N.; Brown, M.; et al. GMES Sentinel-1 mission. *Remote Sens. Environ.* **2012**, *120*, 9–24. [CrossRef]
24. Fernández, M.; Peter, H.; Arnold, D.; Duan, B.; Simons, W.; Wermuth, M.; Hackel, S.; Fernández, J.; Jäggi, A.; Hugentobler, U.; et al. Copernicus Sentinel-1 POD reprocessing campaign. *Adv. Space Res.* **2022**, *70*, 249–267.
25. Masek, J.G.; Wulder, M.A.; Markham, B.; McCorkel, J.; Crawford, C.J.; Storey, J.; Jenstrom, D.T. Landsat 9: Empowering open science and applications through continuity. *Remote Sens. Environ.* **2020**, *248*, 111968. [CrossRef]
26. Gorelick, N.; Hancher, M.; Dixon, M.; Ilyushchenko, S.; Thau, D.; Moore, R. Google Earth Engine: Planetary-scale geospatial analysis for everyone. *Remote Sens. Environ.* **2017**, *202*, 18–27. [CrossRef]
27. Yu, C.; Li, Z.; Penna, N.T.; Crippa, P. Generic Atmospheric Correction Model for Interferometric Synthetic Aperture Radar Observations. *J. Geophys. Res. Solid Earth* **2018**, *123*, 9202–9222. [CrossRef]
28. Yu, C.; Penna, N.T.; Li, Z. Generation of real-time mode high-resolution water vapor fields from GPS observations. *J. Geophys. Res. Atmos.* **2017**, *122*, 2008–2025. [CrossRef]
29. Farr, T.G.; Rosen, P.A.; Caro, E.; Crippen, R.; Duren, R.; Hensley, S.; Kobrick, M.; Paiton, M.; Rodriguez, E.; Roth, D.; et al. The Shuttle Radar Topography Mission. *Rev. Geophys.* **2007**, *45*, RG2004. [CrossRef]
30. National Earthquake Data Center (NEDC). Available online: https://data.earthquake.cn (accessed on 2 November 2025).
31. Costantini, M. A novel phase unwrapping method based on network programming. *IEEE Trans. Geosci. Remote Sens.* **1998**, *36*, 813–821. [CrossRef]
32. Xie, S.; Jin, F.; Krishnan, S.; Sattler, R.J. Signal feature extraction by multi-scale PCA and its application to respiratory sound classification. *Med. Biol. Eng. Comput.* **2012**, *50*, 759–768. [CrossRef] [PubMed]
33. Xu, H. A remote sensing index for assessment of regional ecological changes. *China Environ. Sci.* **2013**, *33*, 889–897.
34. Whittaker, R.H. Gradient analysis of vegetation. *Biol. Rev.* **1967**, *42*, 207–264. [CrossRef]
35. Tomlin, C.D. *Geographic Information Systems and Cartographic Modeling*; Prentice Hall: Englewood Cliffs, NJ, USA, 1990.
36. Connell, J.H. Diversity in Tropical Rain Forests and Coral Reefs. *Science* **1978**, *199*, 1302–1310. [CrossRef]
37. Anselin, L. Local Indicators of Spatial Association—LISA. *Geogr. Anal.* **1995**, *27*, 93–115. [CrossRef]

38. Hanssen, R.F. *Radar Interferometry: Data Interpretation and Error Analysis*; Kluwer Academic Publishers: Dordrecht, The Netherlands, 2001.
39. Wang, J.; Liu, D.; Ma, J.; Cheng, Y.; Wang, L. Development of a large-scale remote sensing ecological index in arid areas and its application in the Aral Sea Basin. *J. Arid Land* **2021**, *13*, 40–55. [CrossRef]
40. Wu, T.; Li, B.; Lian, L.; Zhu, Y.; Chen, Y. Assessment of the combined risk of drought and high-temperature heat wave events in the North China Plain during summer. *Remote Sens.* **2022**, *14*, 4588. [CrossRef]
41. Ding, T.; Yuan, Y.; Zhang, J.; Gao, H. 2018: The Hottest Summer in China and Possible Causes. *J. Meteorol. Res.* **2019**, *33*, 577–592. [CrossRef]
42. Lu, C.; Ye, J.; Wang, S.; Yang, M.; Li, Q.; He, W.; Qin, Y.; Cai, J.; Mao, J. An unusual heat wave in North China during midsummer, 2018. *Front. Earth Sci.* **2020**, *8*, 238. [CrossRef]
43. Huang, J.; Hu, B.; Tan, X.; Cheng, J.; Li, L. Concept and Practice of Open-pit Mining Area Restoration and Reuse—Taking an Open-pit Coal Mining Area in Datong, Shanxi as an Example. *E3S Web Conf.* **2020**, *145*, 02014.
44. Wang, J.; Wang, J. A modified soil-adjusted vegetation index obtained from satellite remote sensing data. *Clim. Environ. Res.* **1997**, *2*, 55–60.
45. Gao, B.C. NDWI—A normalized difference water index for remote sensing of vegetation liquid water from space. *Remote Sens. Environ.* **1996**, *58*, 257–266. [CrossRef]
46. Xu, H. A new index for delineating built-up land features in satellite imagery. *Int. J. Remote Sens.* **2008**, *29*, 4269–4276. [CrossRef]
47. Roy, P.S.; Rikimaru, A.; Miyatake, S. Tropical forest cover density mapping. *Trop. Ecol.* **2002**, *43*, 39–47.
48. Chander, G.; Markham, B.L.; Helder, D.L. Summary of current radiometric calibration coefficients for Landsat MSS, TM, ETM+, and EO-1 ALI sensors. *Remote Sens. Environ.* **2009**, *113*, 893–903. [CrossRef]
49. Sobrino, J.A.; Jiménez-Muñoz, J.C.; Paolini, L. Land surface temperature retrieval from LANDSAT TM 5. *Remote Sens. Environ.* **2004**, *90*, 434–440. [CrossRef]

Disclaimer/Publisher's Note: The statements, opinions and data contained in all publications are solely those of the individual author(s) and contributor(s) and not of MDPI and/or the editor(s). MDPI and/or the editor(s) disclaim responsibility for any injury to people or property resulting from any ideas, methods, instructions or products referred to in the content.